Multi-Dimensional Characterization of Battery Materials

Ralf F. Ziesche, Thomas M. M. Heenan, Pooja Kumari, Jarrod Williams, Weiqun Li, Matthew E. Curd, Timothy L. Burnett, Ian Robinson, Dan J. L. Brett, Matthias J. Ehrhardt, Paul D. Quinn, Layla B. Mehdi, Philip J. Withers, Melanie M. Britton, Nigel D. Browning, and Paul R. Shearing*

Demand for low carbon energy storage has highlighted the importance of imaging techniques for the characterization of electrode microstructures to determine key parameters associated with battery manufacture, operation, degradation, and failure both for next generation lithium and other novel battery systems. Here, recent progress and literature highlights from magnetic resonance, neutron, X-ray, focused ion beam, scanning and transmission electron microscopy are summarized. Two major trends are identified: First, the use of multi-modal microscopy in a correlative fashion, providing contrast modes spanning length- and time-scales, and second, the application of machine learning to guide data collection and analysis, recognizing the role of these tools in evaluating large data streams from increasingly sophisticated imaging experiments.

1. Introduction

In recent years, the demands for low carbon energy storage in the transport and grid sectors has driven a global research effort in the development and optimization of Li-ion batteries (LIB) with increasing demands on cost, energy, and power density, and operational safety. In tandem, a broad palette of microscopy and associated simulation and analysis tools, has provided a platform for increasingly sophisticated analysis with resolutions spanning the atom to the device level. These tools increasingly extend investigations into the third dimension, providing

R. F. Ziesche, T. M. M. Heenan, P. Kumari, J. Williams, W. Li, M. E. Curd, T. L. Burnett, I. Robinson, D. J. L. Brett, M. J. Ehrhardt, P. D. Quinn, L. B. Mehdi, P. J. Withers, M. M. Britton, N. D. Browning, P. R. Shearing
The Faraday Institution
Quad One
Harwell Science and Innovation Campus
Didcot OX11 0RA, UK
E-mail: p.shearing@ucl.ac.uk
R. F. Ziesche, T. M. M. Heenan, D. J. L. Brett, P. R. Shearing
Electrochemical Innovation Lab
Department of Chemical Engineering
UCL
London WC1E 7JE, UK
R. F. Ziesche, P. D. Quinn
Diamond Light Source Ltd
Harwell Science and Innovation Campus
Didcot OX11 0DE, UK

R. F. Ziesche
Helmholtz-Zentrum Berlin für Materialien und Energie
Hahn Meitner Platz 1, 14109 Berlin, Germany
P. Kumari, M. M. Britton
School of Chemistry
University of Birmingham
Birmingham B15 2TT, UK
J. Williams, M. J. Ehrhardt
Department of Mathematical Sciences
University of Bath
Bath BA2 7AY, UK
M. E. Curd, T. L. Burnett, P. J. Withers
Henry Royce Institute
Department of Materials
The University of Manchester
Oxford Road, Manchester M13 9PL, UK
I. Robinson
Department of Physics and Astronomy
UCL
London WC1E 6BT, UK
W. Li, L. B. Mehdi, N. D. Browning
Department of Mechanical
Materials and Aerospace Engineering
University of Liverpool
Liverpool L69 3GH, UK
M. J. Ehrhardt
Institute for Mathematical Innovation
University of Bath
Bath BA2 7AY, UK

**ADVANCED
SCIENCE NEWS**

www.advancedsciencenews.com

**ADVANCED
ENERGY
MATERIALS**

www.advenergymat.de

Table 1. Comparison of multi-modal imaging characterization with typical reference values.

Technique	MRI	Neutron	X-ray (micro)	X-ray (nano)	FIB-SEM	TEM
Sample size	3–20 mm	1 mm to 50 cm	500 µm to 5 cm	50 to 500 µm	10 µm to 1 mm	100 nm to 500 µm
Sample preparation	Moderate	Easy	Easy to moderate	Difficult	Difficult	Very difficult
Image resolution	30 µm	10 to 300 µm	1 to 100 µm	10 to 300 nm	nm to µm	Å to nm
In situ/operando	Possible	Easy	Easy to moderate	Difficult	Very difficult	Moderate

spatially resolved insight into energy storage materials and devices from the nano- to the millimeter length-scales providing unprecedented understanding of the relationship between electrode microstructure and device performance. Moreover, the opportunity to study materials in their native state (such as within functioning commercial battery cells) and over the fourth dimension (time), through the application of non-destructive in situ and operando techniques is emerging, enabling the exploration of time resolved processes as a function of current, voltage, thermal history, and cycle life.

Electrochemical devices are assembled with complex hierarchical microstructures designed to optimize the electrochemical, thermal, and mechanical performance. For instance, commercial Li-ion cells are assembled, at present, out of a positive and negative electrode which are separated by a porous, typically polymer, separator membrane submersed in a liquid electrolyte. The positive electrodes are manufactured with crystallographic structures that permit desirable (de)lithiation, then these primary crystalline particles are typically scaled into secondary agglomerates that are mixed with a carbon-binder-domain (CBD) matrix, printed and pressed/calendared onto a current collector to form the electrode. At the negative electrode, graphite is the ubiquitous active material, where characteristically heterogeneous graphite particles are combined with mechanical, and conductivity enhancing additives and printed in a similar fashion. With increasing need for enhanced energy density, there is a trend toward the addition of Si/SiO_x which display higher gravimetric capacity, but require alternative formulations to account for differences in their mechanical and electrical behavior. At a larger scale, this electrode-separator-electrode assembly is then manufactured into a particular cell format, for example, cylindrical, pouch, or prismatic, for operation. The methods we discuss here are collectively capable of analyzing across the length and time scales critical to battery performance.

In this review, we explore the importance of correlative approaches in examining the multi-length-scale structures (electronic, crystal, nano, micro, and macro) involved in determining key parameters associated with battery operation, degradation, and failure. In doing so, we identify the major achievements and future challenges for a broad range of imaging tools. First a brief summary is provided (organized by technique and length scale) of recent progress in characterizing energy storage materials and devices achieved by magnetic resonance, neutron, X-ray, focused ion beam (FIB), scanning (SEM) and transmission electron (TEM) microscopy. We recognize the breadth of additional characterization tools that are widely applied to battery materials and devices, and focus here on the aforementioned techniques, first due to their common microscopy theme, and second due to their ability to be

effectively correlated as part of a multi-scale imaging framework.

From this portfolio of microscopy tools, each individual technique offers unique benefits and drawbacks. The trade-off between spatial resolution and sample size is, perhaps, the most widely recognized compromise in microscopy, which is considered alongside the relative difficulties in sample preparation and capability for operando measurements in the **Table 1**.

The myriad processes that govern battery performance and lifetime mandate a multiple length scale understanding; from atomic re-structuring and interphase growth at the finest scales, through electrode morphology governing energy and power density at the micro-scale, to the macroscopic spatial trends associated with cell engineering and safety. Key examples from the literature are used to illustrate the current state-of-the-art in the application of these characterization tools to tackle these challenges.

By reflecting on recent progress we identify two major trends which are explored later in this paper: first, the use of correlative multi-modal microscopy in providing multiple contrast modes and analytical information, spanning length- and time-scales, and second, the application of computational imaging and machine learning (ML) tools to guide data collection and analysis, recognizing the role of these tools to evaluate large data streams from increasingly sophisticated imaging experiments. Finally, we summarize future opportunities.

A significant focus of this review is on state-of-the-art, in situ and operando non-destructive characterization techniques, which have emerged in recent years as powerful tools for battery research and design. In situ tools are defined here as those which have the capability to study the battery in its native state, whilst operando tools are those which can characterize a battery during operation (for example during current flow). In both instances, the trade-off between the analysis volume and the achievable resolution remains but as these families of techniques permit repeat study of the identical sample (either during or after operational cycling), direct (rather than statistical) quantification of microstructural or chemical evolution can be achieved. These are complemented by ex situ characterization techniques which remain important in the arsenal of available tools. Here particular care must be exercised to ensure the statistical significance of the sample selected for analysis, and the risk of damage to the sample during preparation also must be considered. Both these factors can be mitigated by linking them to the above non-destructive techniques. Moreover, new possibilities for correlative multi-scale characterization can help to break the microscopy paradigm wherein high spatial resolution is achieved at the expense of sampling volume and wider context, which is considered, alongside computational imaging and machine learning as a key emerging opportunity in later sections of this article.

**ADVANCED
SCIENCE NEWS**

www.advancedsciencenews.com

**ADVANCED
ENERGY
MATERIALS**

www.advenergymat.de

2. Magnetic Resonance Imaging/Electron Paramagnetic Resonance Imaging

Magnetic resonance imaging (MRI) is a non-destructive characterization technique, providing spatially resolved information on the atomic environment of nuclear magnetic resonance (NMR) active nuclei, such as ^1H, ^{19}F, ^7Li, or ^{23}Na.[1–3] MRI can penetrate optically opaque samples, but is unable to image samples encased in metal, because radio frequency (RF) radiation cannot penetrate metals beyond a skin depth $\approx 10^{-5}$ m.[4] Which makes the sample preparation challenging and limits the material useable for battery cells to principally plastic housings. Moreover, the presence of metals can introduce image artifacts, but are minimized through sample alignment with RF and magnetic fields.[5,6] In the last decade, in situ and operando MRI have been developed to provide time-resolved quantitative information about chemical changes within electrodes and electrolytes, enabling a more holistic view of battery chemistry[6–8] (**Figure** 1a). While MRI has lower spatial resolution (typically $\geq 10^{-5}$ m) than some other imaging techniques, the combination of NMR spectroscopy and imaging enables the identification, distribution and transport of species across multiple length scales, in 3D, and in real-time.[2] For example, the NMR chemical shift is able to distinguish between metallic and solvated lithium and sodium species, enabling selective observation of changes in the electrolyte and electrodes during electrochemical cycling.[3,5] It is also possible to distinguish mossy or dendritic microstructures.[9] Li dendrites have been visualized by 2D and 3D ^7Li MRI and 3D chemical shift imaging (Figure 1b).[10] In addition to the visualization of dendrites, quantitative information on diffusivity and transport numbers during charge cycling have been acquired using 1D ^7Li MRI.[11] More recently, the formation of sodium dendrites have been visualized, operando, by 2D ^{23}Na MRI and 3D ^1H MRI[5] in a sodium metal cell, and the formation and evolution of metallic and quasi-metallic sodium during the formation cycle, has been followed in a sodium full cell.[5] In situ 1D ^{23}Na MRI has been used to observe the formation and evolution of dendritic and mossy sodium microstructures during deposition and stripping processes.[12]

It is also possible to indirectly observe battery chemistry, using ^1H or ^{19}F MRI of the electrolyte.[13,14] Negative images from ^1H MRI of the electrolyte have be used to reveal lithium or sodium dendrites on the surface of electrodes following galvanostatic plating (Figure 1c).[5,14] ^1H MRI of the electrolyte has also proved useful observing battery chemistries involving NMR inactive, or low receptivity, nuclei, and has been successfully used to observe the distribution and speciation of zinc-oxygen electrochemistry in a zinc-air battery[4] as shown in Figure 1d. Internal changes in the magnetic susceptibility of electrodes, associated with a battery's charge state, have been detected using "inside-out" MRI, by observing changes in the magnetic field map surrounding a battery using water as detection medium, during charge cycling.[15] Dynamic nuclear polarization (DNP) enhanced NMR achieves up to several orders of magnitudes higher sensitivity and selectivity by microwave enhanced nuclear magnetization. Hope et al.[16] reports the significant hyperpolarization of room temperature ^7Li NMR signal of cycled lithium metal anodes using high-field room temperature Overhauser DNP enable studying spectra of solid-electrolyte interphase (SEI) species selectively.

Electron paramagnetic resonance imaging (EPRI) relies on the detection of electron spins offering higher sensitivity than MRI. In situ EPRI has been used to monitor battery chemistry in a LIB using $Li_2Ru_{0.75}Sn_{0.25}O_3$ and Li electrode allowing the stripping/plating of Li metal to be visualized and the nucleation of Ru_5/oxygen species to be located.[17] Using cells constructed from Perfluoroalkoxy alkanes, which are transparent to microwaves.[18] EPRI has also been used to provide time resolved semi-quantitative information on the formation and growth of lithium dendrites.[19] Further, semi-quantitative distributions of Li deposition have been determined using an anode-free cell via in situ spatial-spatial EPRI where Li deposit sizes could be estimated by spectral-spatial EPRI.[20] Dutoit et al.[21] show the benefit of in situ correlative EPR spectroscopy and EPRI to track the nucleation of sub-micrometric Li particles and dendrites formed through the separator in a symmetric $Li|LiPF_6|Li$ cell as shown in Figure 1e. However, EPRI suffers from several technical challenges and the typically broad line widths associated with the EPR signal makes image reconstruction more challenging than MRI.[22]

3. Neutron Imaging

The contrast in neutron imaging is based upon the interaction of thermal (≈ 1.0–2.5 Å wavelength) or cold (>2.5 Å) neutrons with the atomic nuclei. The coherent scattering (diffraction) provides information about the crystal structure of the sample. The attenuation of neutrons does not follow a systematic relationship down the periodic table and can vary significantly, even between the isotopes of one element. Therefore, imaging with neutrons allows non-destructive studies of bulky metallic samples (which are easily penetrated) while providing a high sensitivity to light elements (such as lithium). Since ^6Li has a much higher absorption cross section than ^7Li, the difference in the isotope cross sections can be exploited, for example, to study the Li^+ diffusion process in Li-ion cells by monitoring the movement of ^6Li through ^7Li.[23,24] Neutron imaging for battery applications has recently been the subject of a comprehensive review[25] but is also briefly considered here alongside other key characterization tools for completeness.

Despite the relatively long exposure times for neutron imaging, varying between seconds/minutes for low/high spatial resolved images (≈ 100 μm and <20 μm), 2D neutron radiography can be used to analyze dynamic Li^+ transport, for instance in pouch cells, where the Li concentration at different state of charge and electrode swelling can be resolved.[26,27] However due to the limited spatial resolution, thick electrodes are often used to achieve meaningful results. Thus, the lithium intercalation and capacity loss in relation to trapped lithium has been studied for 300 μm thick graphite composite electrodes.[28] Further, this method is also well suited to examine the influence of the current density on the Li transport and capacity. The influence of different C-rates (measure of the dis-/charge current relative to the cell capacity A Ah^{-1}) in >600 μm $Li_{4+y}Ti_5O_{12}|LiCoO_2$ electrodes has been demonstrated whereby high C-rates generate a lower capacity and Li transport could only be found in the electrode layers close to the separator.[29,30] A combination of operando neutron radiography and in situ neutron CT has been used to examine the Li dendrite growth inside a $^7Li|LiMn_2O_4$ cell.[31] The higher
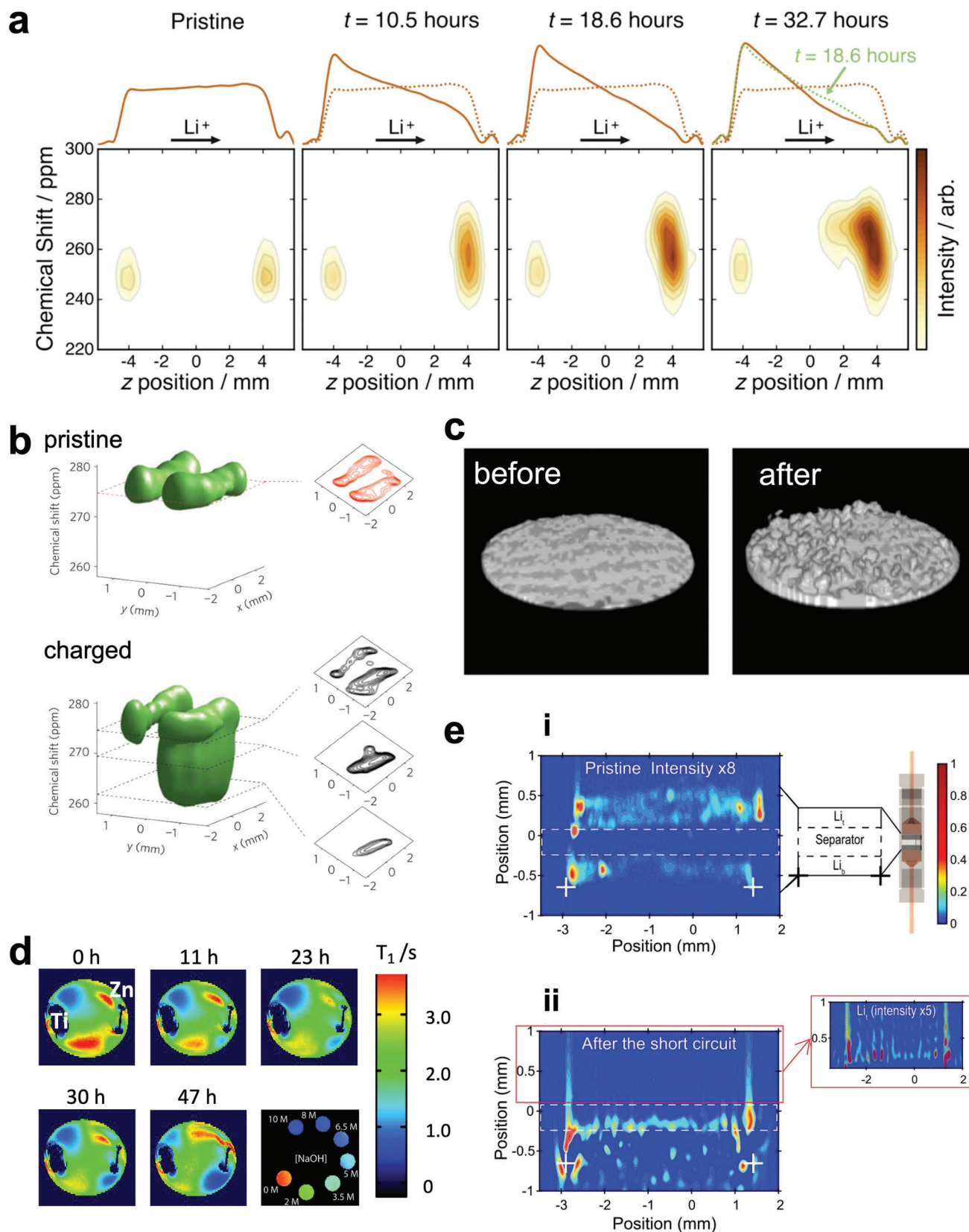
Figure 1. MRI imaging. a) MRI in situ study on a symmetric Li cell shows the evolution of ^7Li electrolyte profile (top) and the ^7Li chemical shift imaging (CSI) of the Li metal electrodes, charged at 0.76 mA cm^{-2}, indicating dendrite growth on the positive electrode. Reproduced with permission.[8]

**ADVANCED
SCIENCE NEWS**

www.advancedsciencenews.com

**ADVANCED
ENERGY
MATERIALS**

www.advenergymat.de

attenuating Li dendrite formation is distinguishable from the less attenuating [7]Li-anode whereby the dynamic growth is captured from the radiographs and the 3D location by the CT scans after each dis-/charge step. Although exposure times for neutron CT are often in the range of hours it provides a unique view inside the Li distribution of, for example, <1 mm thick V_2O_5 electrodes in commercial coin cells[32] or visualizing the variation of the discharge products across the bulk of lithium-air batteries.[33]

The latest advances complement neutron imaging with X-ray imaging to examine both light and heavy elements. As demonstrated on a spirally-wound CR2 Li|MnO_2 primary cell using operando X-ray and in situ neutron CT.[34] X-rays primarily show the MnO_2 electrode cracking/movement, while neutrons expose the Li intercalation and electrolyte consumption (**Figure 2**a). By using a virtual electrode unrolling technique the electrode movement and Li diffusion is better visualized. Advanced detectors and instruments have enabled the first operando neutron CT and quantification of the Li consumption from the Li-anode in Li|$SOCl_2$ cells with exposure times far below 1 h (Figure 2b).[35,36]

Neutron imaging is highly sensitive to hydrogen making it a favorable technique to study the electrolyte decay visible as gas bubbles. Using neutron radiography, different gel-type electrolytes (e.g., polyvinylidene fluoride) could be characterized by their percentage levels of evolved gas on the graphite electrode.[37] The increased production of bubbles and channels indicates gas evolution (Figure 2c). Moreover, gas evolution has been effectively characterized via a combination of neutron radiography (in 2D) with differential electrochemical mass spectroscopy (DEMS) and prompt gamma activation analysis.[38–40] Neutron imaging studies of other working ions such as Zn^+ are rare due to the low sensitivity of the elements, but provides meaningful results for the electrolyte distribution by due to H.[41,42] Neutron diffraction has been used to study the structural evolution during Li^+ de-/intercalation in Li-ion electrodes, and can also be combined with neutron imaging. A 3D diffraction technique was developed to determine the homogeneity of the Li distribution throughout spiral wound cells in terms of the lattice spacing (d) change of the graphite within a gauge volume of several cubic-millimeters.[43] Bragg edge neutron imaging can combine direct probing of a sample in real space with the collection of structural information from the active crystalline material at the micrometer length-scale.[44] It has been used to examine the lithiation stages of graphite in a LIB pouch cell via analysis of the Bragg edges, from the coherent scattered beam, over the neutron energy spectrum.[45] Bragg edge tomography (3D spatially and energy resolved) has been demonstrated on ultra-thick, directional ice templated, graphite electrodes.[46] Energy resolved tomograms were reconstructed from a set of energy-specific radiographic projections. The (hkl) Bragg edges for graphite were analyzed and the phases reconstructed as 3D volumes (Figure 2d).

4. X-ray Imaging and Spectroscopy

X-rays predominantly interact with the electron cloud surrounding the atomic nucleus and for characterization, energies in the range of 0.1–320 keV are typically employed. These elastic and inelastic X-ray interactions can produce data on the material's macro-, micro-, nano-, crystal-, and electronic-structure, as well as the chemical and elemental compositions. Moreover, spatially-resolved information can be obtained across multiple dimensions. 2D imaging involves either the full-field illumination of a stationary sample or a raster by moving the sample relative to the incident beam to generate a map. As for neutron CT 3D reconstructions require 2D measurements from multiple (hundreds to thousands) points of view to generate a CT image volume.[30] 2D imaging frame rates can vary from microseconds to minutes enabling 4D imaging with 3D image frame rates running from sub-second to hours.[47]

X-rays are often classified according to their source—laboratory or synchrotron. Lab X-ray tubes produce characteristic X-rays of specific energies in relation to the atomic number of the tube's anode, along with a broad energy spectrum of Bremsstrahlung X-rays. Synchrotron radiation is produced by insertion devices (e.g., undulators) that alter the trajectory of ultra-relativistic electrons, producing either broad or (essentially) monochromatic beams of X-rays, depending upon the beam refinement. Generally, lab-based X-ray sources are more easily accessible, but have considerably lower brilliance, hence have longer scanning times, prohibiting very high frame rate in situ and operando studies. Moreover, beam refinement, for example, collimation, energy filtering, etc., is also less common due to the limited flux and broader beam energies. Although, developments in recent years have produced quasi-monochromatic beams and the use of focusing optics such as zone-plates that produce spatial resolutions comparable to equivalent set-ups at synchrotrons.[48,49] Access to X-rays at international synchrotron sources produce substantially higher data rates, enabling imaging of rapid timescale phenomena, as well as allowing more complex combinations of imaging, spectroscopy, and diffraction. Many of these advanced techniques are enabled by the ability to produce small beam sizes, for example, with sub-micron spot sizes, and/or monochromatic incident X-ray energies, for example, only X-rays with wavelengths within a particular range of values.[47]

The X-ray source can illuminate the sample with a cone beam (typical of lab sources) or a parallel beam (typical of synchrotron sources). The great majority of X-ray imaging is based on beam attenuation by a sample that is fully illuminated by the incident beam, with the transmitted beam interactions recorded on a detector producing a radiograph projection (transmission X-ray microscopy, TXM). For instance, 2D radiography has been

Copyright 2015, ACS. b) [7]Li CSI of the pristine and the charged cell reveals the formation of Li microstructure on the negative electrode. Reproduced with permission.[10] Copyright 2012, Springer Nature. c) Negative space images from 3D ^{1}H MRI of Na before and after galvanic plating showing dendrite grow. Reproduced with permission.[5] Copyright 2020, Nature Communications. d) Horizontal ^{1}H MRI T_1 maps of a full Zn-air cell containing 1 M NaOH solution. The cell contains unconnected Ti and Zn stripes under constant load discharge at 12 kΩ, shown at different acquisition times and a reference measurement. Reproduced with permission.[4] Copyright 2013, ACS. e) In situ spatial-spatial EPRI recorded in i) the pristine state and ii) after short circuit, respectively. The intensity crossing the separator suggesting the location of dendritic Li after the short circuit. Reproduced with permission.[21] Copyright 2021, Springer Nature.
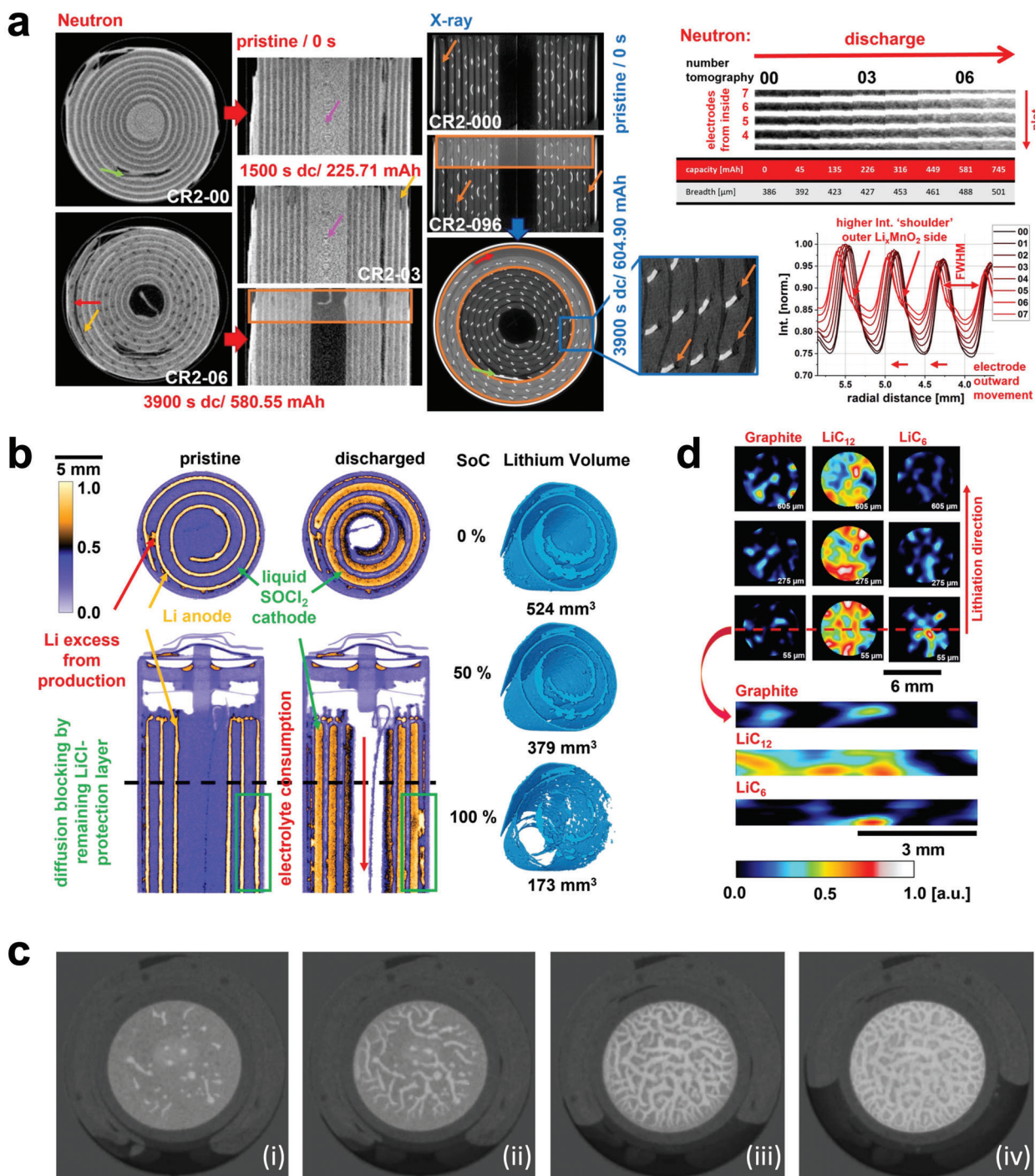
2300103 (5 of 20)

Figure 2. Neutron imaging. a) Orthogonal slices of neutron and X-ray CT scans of a CR2 Li|MnO₂ primary cell, at different SoC, demonstrate the complementarity of both kinds of rays. Neutrons unravel the electrochemical changes such as Li diffusion/consumption (yellow arrows) and electrolyte consumption (purple), where X-rays visualize mainly structural changes such as cracking (orange) and movement (red) of the MnO_2 electrode or high attenuating metallic parts (green). A virtual electrode unrolling shows cut-outs of the unrolled multilayer electrode sections showing volume expansion of MnO_2 and electrode movement (right). Reproduced with permission.[34] Copyright 2020, Springer Nature. b) Lithium mass transport from the lithium metal anode to the liquid thionyl chloride cathode of Li|SOCl₂ ER14505M cell discharged with 100 mA as orthogonal slices from operando neutron CT, alongside with the quantified lithium anode depletion. Reproduced with permission.[36] Copyright 2020, IOP. c) Neutron radiographs show the gas evolution in a graphite|LiMn₂O₄ cell with EC:PC 2:3 1Mм LiClO₄ electrolyte during the first charge from (i) to (iv). Reproduced with permission.[37] Copyright 2004, Journal of Power Sources. d) Horizontal and vertical maps of the lithiation states graphite, LiC₁₂, and LiC₆ of an ice templated graphite electrode at 33% SoC using neutron Bragg edge imaging. The 3D reconstructions indicate inhomogeneous phase distributions with the highest lithiation degree close to the lithium-metal counter electrode. Reproduced according to the terms of the C-CBY license.[46] Copyright 2020, The authors, published by MDPI.
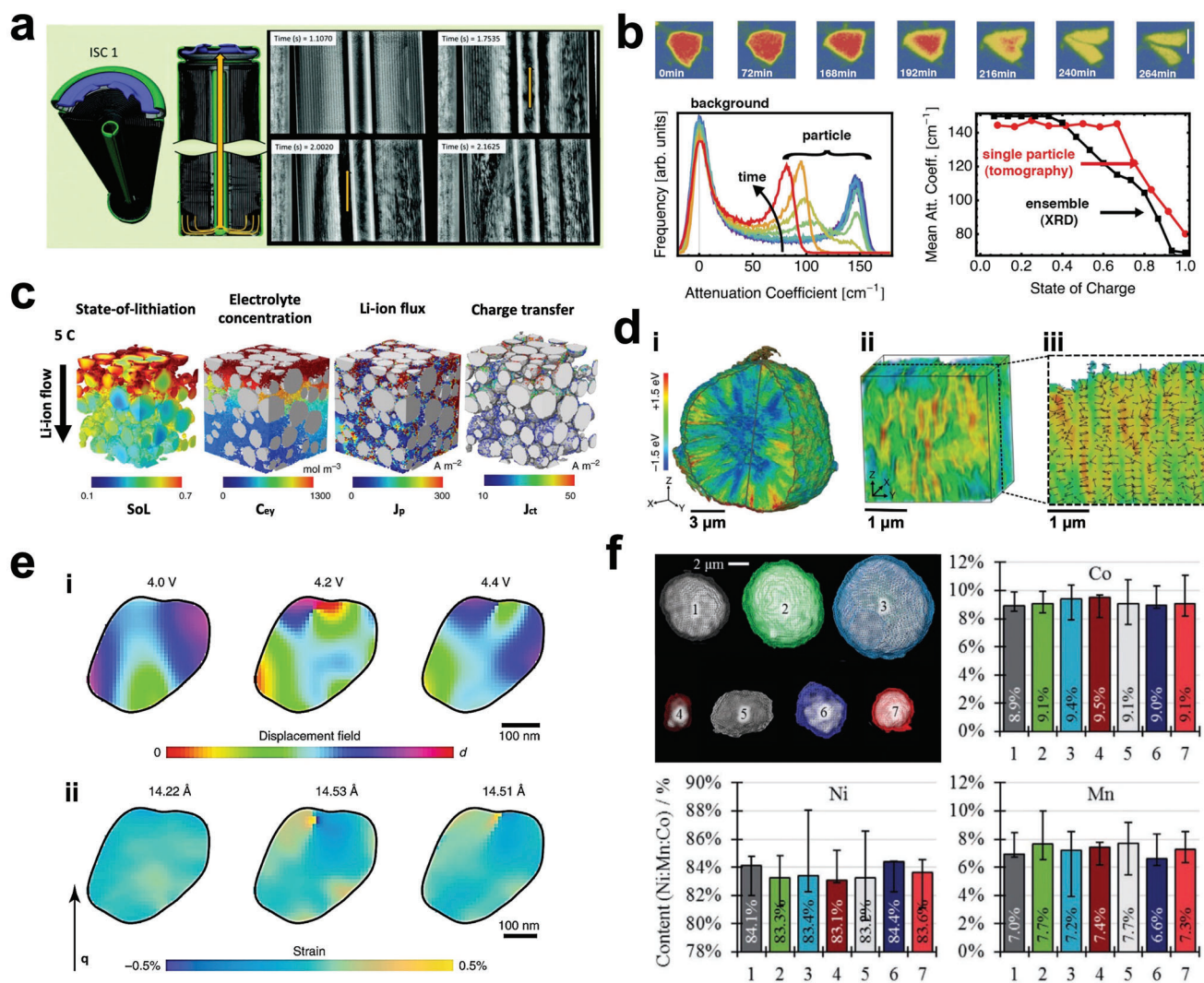
Figure 3. X-ray imaging and mapping. a) Characterizing thermal runaway within an 18 650 Li-ion cell by inducing and monitoring internal short circuits. 3D illustration and time-stamped radiographs showing the predicted path of gas flow through the core of the cell, etc. Reproduced with permission.[50] Copyright 2017, RSC. b) Synchrotron X-ray CT visualization of different internal structure and phase transformation kinetics in dense Sb-Ti particles. Attenuation coefficient histogram show the density transformation from high to low and the mean attenuation coefficient of the CT is compared with that of operando XRD for various SoC. Reproduced with permission.[67] Copyright 2015, Wiley-VCH. c) An example of advanced computational modelling conducted on X-ray CT data, so-called image-based modelling. Simulated discharge of the reconstructed NMC111 cathode and an ideal lithium anode (half-cell) at 5 C. Reproduced with permission.[83] Copyright 2020, Springer Nature. d) Charge distribution guided by crystallographic grain orientations in polycrystalline NMC using XANES-CT. i–iii) 3D Ni valence state distribution, representative region from and 2D nano-domain valence gradient of the rod-NMC. Reproduced with permission.[90] Copyright 2020, Springer Nature. e) In situ evolution of a NCA nano-particle during charging imaged by BCDI. (i) and (ii) showing the displacement field and strain along the (001) direction. Reproduced with permission.[92] Copyright 2018, Springer Nature. f) Quantifying the elemental ratio of Co, Ni, and Mn in seven single NMC811 particles that have been cycled to 4.5 V using XRF. Reproduced with permission.[49] Copyright 2020, Wiley-VCH.

employed to study cylindrical and pouch[50–54] cells during abuse testing. Moreover, by rotating the samples, time resolved 3D analysis during cell cycling[55,56] and failure[50,57] (**Figure 3**a) have been studied.

According to the available optics, the spatial resolution can be varied from hundreds of microns to tens of nanometers although the field of view tends to decrease in parallel from hundreds of millimeters to tens of microns, respectively.[30] The 3D features of various battery material and chemistries have been examined, from commercial standards such as graphite (Gr)[58,59] to

less-common alternatives such as LiVO$_2$[60] and Sn[61] Moreover, the constituents of composite materials can be distinguished due to their differing X-ray interactions, for example, LiCoO$_2$ with LiNi$_{1/3}$Mn$_{1/3}$Co$_{1/3}$O$_2$ (NMC111)[62] and even single particles of NMC111, LiNi$_{0.8}$Co$_{0.15}$Al$_{0.05}$O$_2$ (NCA)[63] and LiNi$_{0.8}$Mn$_{0.1}$Co$_{0.1}$O$_2$ (NMC811) have been successfully identified.[64]

3D methods are particularly useful to study novel and complex microstructures. For instance, sponges have been assessed for Zn-based batteries,[65] hollow-carbon-sphere/MnO$_x$ has been evaluated for Li-S batteries,[66] and Sb-Ti particles with

elevated internal porosities have demonstrated increased fracture resilience,[67] see Figure 3b.

Some materials are known to undergo detrimental structural changes during electrochemical operation, for instance Si undergoes a significant volume expansion and contraction[68,69] and Li metal dendrites that can grow under harsh conditions, visualized in liquid ($LiPF_6$),[70] and solid electrolytes.[71–73] It should be noted that within degradation studies, which are often the focus of many X-ray imaging investigations, when using synchrotrons care must be taken during characterization to ensure that the sample is not damaged via radiation exposure, for example, deterioration of the carbon binder .[74] This can be achieved by minimizing the dose and optimizing the incident beam energy. Imaging light elements such as lithium is challenging due to the lack of contrast produced through the weak X-ray attenuation, due to the low number of electrons orbiting the small nuclei. However, phase contrast can be used to enhance edge features, as demonstrated on separators by Finegan et al.[75] but it can be advantageous to combine complementary X-ray and neutron imaging to explore very light elements such as H_2/H^+ or Li/Li^+[34] because, as discussed earlier, neutron scattering is dominated by nuclear (as opposed to electron) interactions, providing excellent correlative insight, see Figure 2a.

Studies linking across the various length scales of electrochemical cells are valuable but require multi-modal imaging and various different sample preparation techniques.[76–79] Such rich multidimensional datasets can be of great value to modelers and experimentalists alike such that it is becoming increasingly more common to release the raw data and procedures via open source repositories and articles.[77,80–82] Such data can feed into highly complex 3D models[82–87] providing unparalleled insight into the electrochemistry at these very small scales, see Figure 3c. Additionally, ptychographic methods are also emerging as powerful alternatives for high-resolution imaging.[88,89]

In addition to traditional X-ray CT imaging, it is possible to create maps using the scattered signals or energy dependent absorption to reveal elemental distributions (by fluorescence), different crystal structures (by diffraction), or charge states (by absorption). For example, the use of multiple incident energies can allow the oxidation state to be mapped in three dimensions via X-ray absorption near edge spectroscopy (XANES-CT); highly informative for the design of guided charge distributions[90] (Figure 3d).

Bragg coherent X-ray Imaging (BCDI) can characterize individual crystals, as demonstrated by the mapping of dislocations within $LiNi_{0.5}Mn_{1.5}O_4$.[91] Li-rich layered oxides $Li_{1.2}Ni_{0.13}Mn_{0.53}Co_{0.13}O_2$[92] (Figure 3e), and NMC811.[93] Hard X-rays are used to study individual cathode grains as a function of charge-state in an operando environment, such as a coin cell. BCDI uses a coherent X-ray beam only available from synchrotron sources and focuses it sufficiently so that only a few grains in the electrode are illuminated. Bragg diffraction leads to a peak which originates uniquely from an individual grain; the X-ray coherence causes this peak to have fine structures in the form of fringes, which can be measured and inverted to images with a resolution approaching 20 nm. BCDI images are complex with amplitude and phase information, seen in Figure 3e, and contain novel information about crystal strain in the phase channel, which is highly sensitive to the lattice distortions associated with dis-/charging.

Moreover, X-ray diffraction CT (XRD-CT) has proven highly valuable in mapping the crystallography throughout electrode microstructures. For instance XRD-CT has revealed heterogeneities within $LiMn_2O_4$[94] whereby differences in particle lithiation have produced a variety of rock-salt, monoclinic and spinel structures. The mapping of S-containing structures within Li-S cells has permitted the proposal of kinetic laws that have been derived from bulk electrode behaviors.[95] The charge-balancing between Si and Gr within composite electrodes could be determined with XRD-CT by examining the kinetics minuets following the transition from operation to open circuit.[96] As well as short-term dynamics, long-duration changes have been explored, for instance within NMC111[97] exposing possible mechanisms for irretrievable capacity loss.

X-ray fluorescence CT can reveal the distribution of the constituent elements which, when correlated to other techniques such as TXM and XRD, can produce a comprehensive picture of the material properties[49] (Figure 3f).

In summary X-ray imaging and related spectroscopy methods have revolutionized our understanding of battery materials and the most valuable of these studies are often cross-correlative in nature, involving several complementary techniques often examining battery behavior in real time.

5. Electron and Focused Ion Beam Techniques

Being charged particles, electrons interact more strongly with matter than neutrons and X-rays, providing significant contrast through different modalities. However, only the near-surface region can be examined using an SEM at moderate energies (0.5–30 keV) or within thin sections (50–300+ nm) using a TEM at high energies (>30 keV). Electron images with resolutions up to ≈1 nm can be formed via the collection of topography-sensitive secondary electrons (SEs), or composition and crystal-sensitive backscattered electrons.[98] Crystallographic information can also be obtained by interpreting the diffraction (through electron backscatter diffraction) of the scattered electrons while chemical information can be added by detecting the emissions of characteristic X-rays (through energy dispersive X-ray spectroscopy, EDS).[98,99] The principal advantage of thin TEM samples is that the greatly reduced beam-sample interaction volume facilitates pre-eminent, atomic-level static/dynamic compositional, and structural analysis in battery materials.[100] Typically, 2D image resolution is on the sub-Angstrom scale in aberration-corrected scanning transmission electron microscopes (STEM), with these microscopes simultaneously allowing chemical components to be mapped by EDS and electron energy-loss spectrometry (EELS) with atomic precision and sensitivity. By using in situ or operando holders, time-resolved morphological and structural changes can be characterized in a native environment under controllable external biases—essentially a working nanobattery can be constructed and studied inside the microscope. More recently, cryogenic methodologies have been used to "freeze in place" specific time points in battery charging cycles to permit high resolution analysis of the beam-sensitive reaction products that are created. Currently, there are many attempts to improve the spatial/temporal resolution and sensitivity of the analysis by using 4D-STEM (ptychography) methods.

**ADVANCED
SCIENCE NEWS**

www.advancedsciencenews.com

**ADVANCED
ENERGY
MATERIALS**

www.advenergymat.de

FIB and laser beam machining tools paired to SEMs[101] in dual or tri-beam configurations allow the fabrication of site-specific samples for TEM or the 3D analysis of materials by block face serial sectioning tomography (SST) in the SEM[102–105] as shown in **Figure 4**a.

Various battery processes, including changes in the SEI layer and the formation of dendrites, can be studied using EM techniques.[106,107] Ex situ SEM imaging (typically achieved via interruption of charge/discharge cycles) has been performed on a variety of battery types. For example, imaging of K-metal anodes revealed a mechanism of dendrite healing triggered by self-heating[108] (Figure 4b). For aluminum battery anodes the importance of an Al_2O_3 oxide layer in suppressing dendrite formation was demonstrated[109] and for Zn batteries, dendrite suppression via electrolytic additives was shown.[110] More recently, in situ and operando SEM/TEM investigations have become more common. Such methods require specialist (electron-beam transparent) test environments but allow battery processes to be observed "live" and without the risk of contamination during transfer to the microscope. In situ/operando SEM/TEM has been used to directly observe the evolution of SEI layers and/or dendrites in various Li-based batteries, including all-solid Li-metal|polymer batteries.[111,112] Li–SnO_2[113] batteries or lithium plating/stripping experiments to study liquid electrolyte additives to suppress dendrites such as $LiNO_3$ and Li_2S_8[114] amongst others.[107] In situ/operando SEM/TEM has also been used to observe the dissolution and redeposition of Li_2S salt in Li|Li_2S–C cells, thereby identifying the type of encapsulating matrix required to improve the performance of the Li_2S cathode[115] (Figure 4c).

Low temperature EM (achieved via LN_2 cooling), known as Cryo-SEM/TEM, can aid in the imaging of beam-sensitive or moisture-containing samples. Thus, Li metal dendrites were shown to be stable under exposure to a relatively high current electron beam in cryo- conditions; allowing superior TEM and SEM resolutions to be achieved.[116] Recently, the benefits of cryogenic FIB techniques for sensitive battery materials, such as Li, has been highlighted[117,118] (Figure 4d). Ion implantation and surface oxidation can be substantially reduced using Cryo-FIB techniques, improving the quality of both extracted TEM samples and the analyses conducted on (serially)-sectioned surfaces.[118]

As mentioned earlier, FIB sectioning can be combined with SEM imaging and/or analysis techniques to perform targeted 2D investigations or 3D SST. For example, 2D investigations of all-solid Li-metal-polymer batteries demonstrated that their dendrites are hollow (≈100 nm wall thickness); with complementary chemical analysis suggesting reduction of the polymer electrolyte during cycling[112] (Figure 4e). Similarly, sectioning of an "isle" formed on an anode surface indicated the decomposition of LiTFSI salt[111] Individual dendrites (from Zn[105,119] or Li[120] electrodes) have been analyzed via 3D SST, with the images revealing various aspects such as the shape, size, orientations, roughness and connectivity of the dendrite branches. The Zn electrode analysis in ref. [105] also revealed significant fracturing of the (polypropylene) separator due to dendritic growth within its micropores. Despite the distinct morphology of these dendrites, connectivity with the surface dendrites was revealed in some cases (Figure 4a), which may indicate that these deposits can act as surface-nucleation sites once the micropores are filled.

A similar study on a Li-rich NMC electrode also revealed fracturing after cycling, due to expansion/contraction of the primary NMC particles due to de-/lithiation (Figure 4f).[121] Studies such as these highlight the potential of SST to reveal the mechanisms of battery degradation. It is likely that greater adoption of SST techniques will yield further insights into battery degradation mechanisms, particularly where multiple SEM modalities are utilized. More advanced sectioning methods, such as Xe$^+$ Plasma-FIB (P-FIB) or femtosecond (fs) -laser systems[122,123] have the potential to substantially increase SST volumes whilst simultaneously improving the quality of the cut surfaces[103,104] (the unsuitability of mechanical preparation for delicate Li dendrites has been noted previously[105]). The benefits of large-volume, multi-modal SST, and the potential to correlate the results with other investigations, have been described in detail elsewhere.[103,124]

Some of the earliest uses of TEM methods to study battery systems involve ex situ high angle annular dark field (HAADF) STEM, with images clearly showing phase transformations and structural changes in for example, the $LiNi_{0.8}Mn_{0.1}Co_{0.1}O_2$ (NMC811) cathode material for LIB.[125] In these results, the pristine NMC811 has a layered rhombohedral R3̄m structure, indicated by the d-spacing of the (003) plane (**Figure 5**a). After cycling, the aged NMC811 nanoparticles show both the open channel and the rock-salt reconstruction near the surface, which can be discerned by the difference in d-spacing. Besides shedding light on the degradation mechanisms of cathode materials[125,126] these STEM methods provide an important and irreplaceable ex situ characterization tool for other battery components, including the anode,[127,128] electrolyte,[129] etc.

In addition, to extensive ex situ characterization of pristine and post cycling battery components, in situ and operando TEM has been widely used in characterizing the changes of battery materials upon external biases in their native environment. Generally, liquid cell[130–132] (Figure 5b), open cell,[133–136] and environmental cell[137,138] (Figure 5c) have been used for different types of batteries. For example, Li deposition and dissolution was studied by using an operando liquid cell for Li based batteries, such as LIB, lithium–sulfur (Li–S), and lithium–air (Li–O_2).[130,131] The liquid cell is an electrochemical three/four electrode system to study battery materials in their native state, as all the battery components can be studied in their electrolyte solution (as, in commercial cells) (Figure 5b). HAADF images (Figure 5d) show the first three cycles of the Li deposition and dissolution processes, where dead Li can be clearly seen at the end of each cycle and SEI layer can be identified at the surface of electrode. The cyclic voltammetry, volume change of the deposited Li, and thickness change of SEI layer can also be quantitatively recorded and correlated directly with structural/compositional changes (Figure 5e).

Compared with the liquid cell, the open and environment cells (Figure 5c) maintain the intrinsic high resolution of TEM.[133] By combining the open cell and an environmental cell, it was found that the oxygen-reduction reaction on a carbon nanotube cathode initially produces LiO_2, which later disproportionate into Li_2O_2 and O_2 for a Li–O_2 battery (Figure 5f).[137] By using this environmental cell, the cathode–air interfacial reaction was found to be driven by the Li-water interaction.[138] Among all the components of air, the water vapor is the only active one which triggers the delithiation process and the formation of LiOH layer (Figure 5g). The growth of a passivation layer stops at a
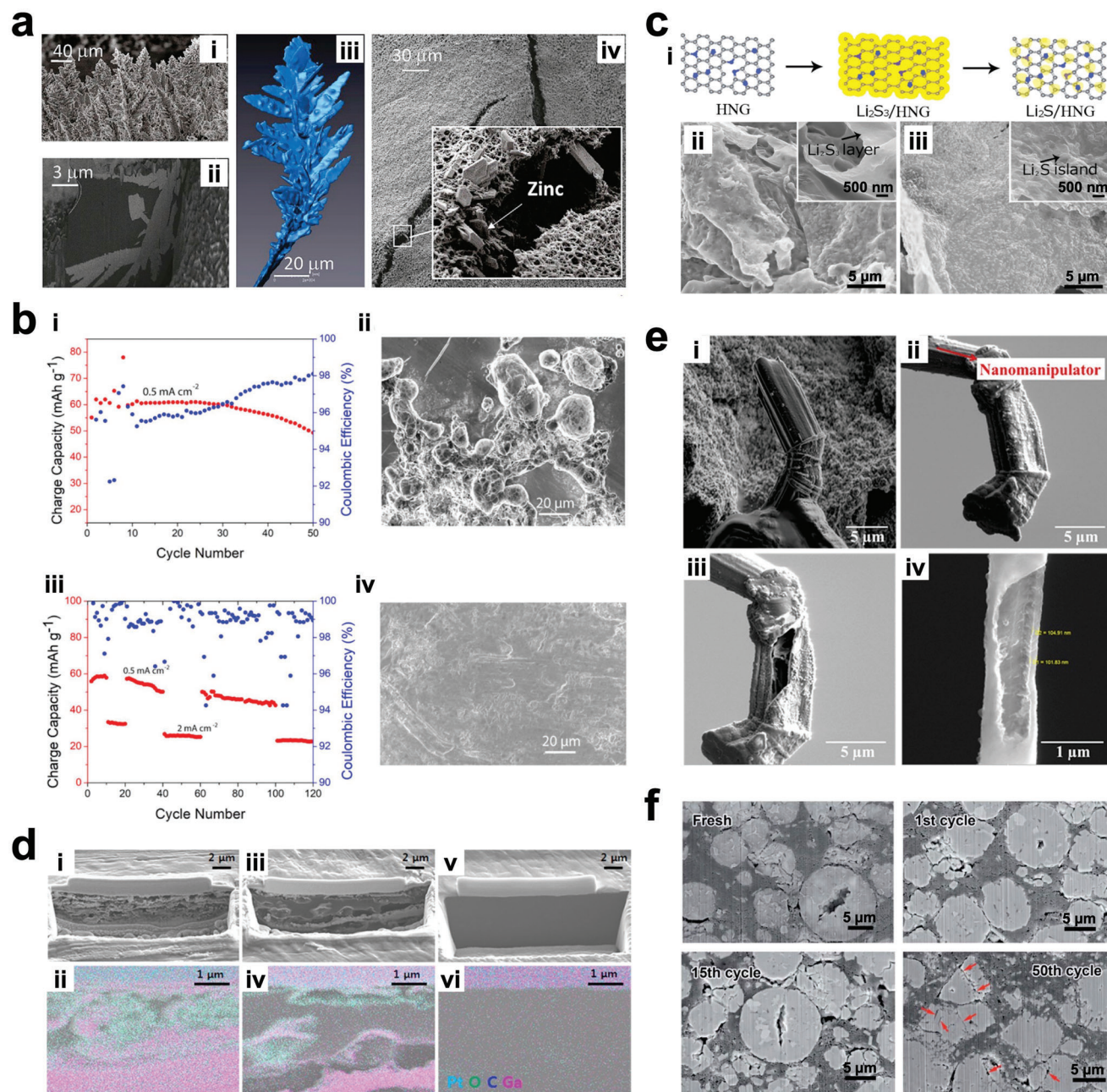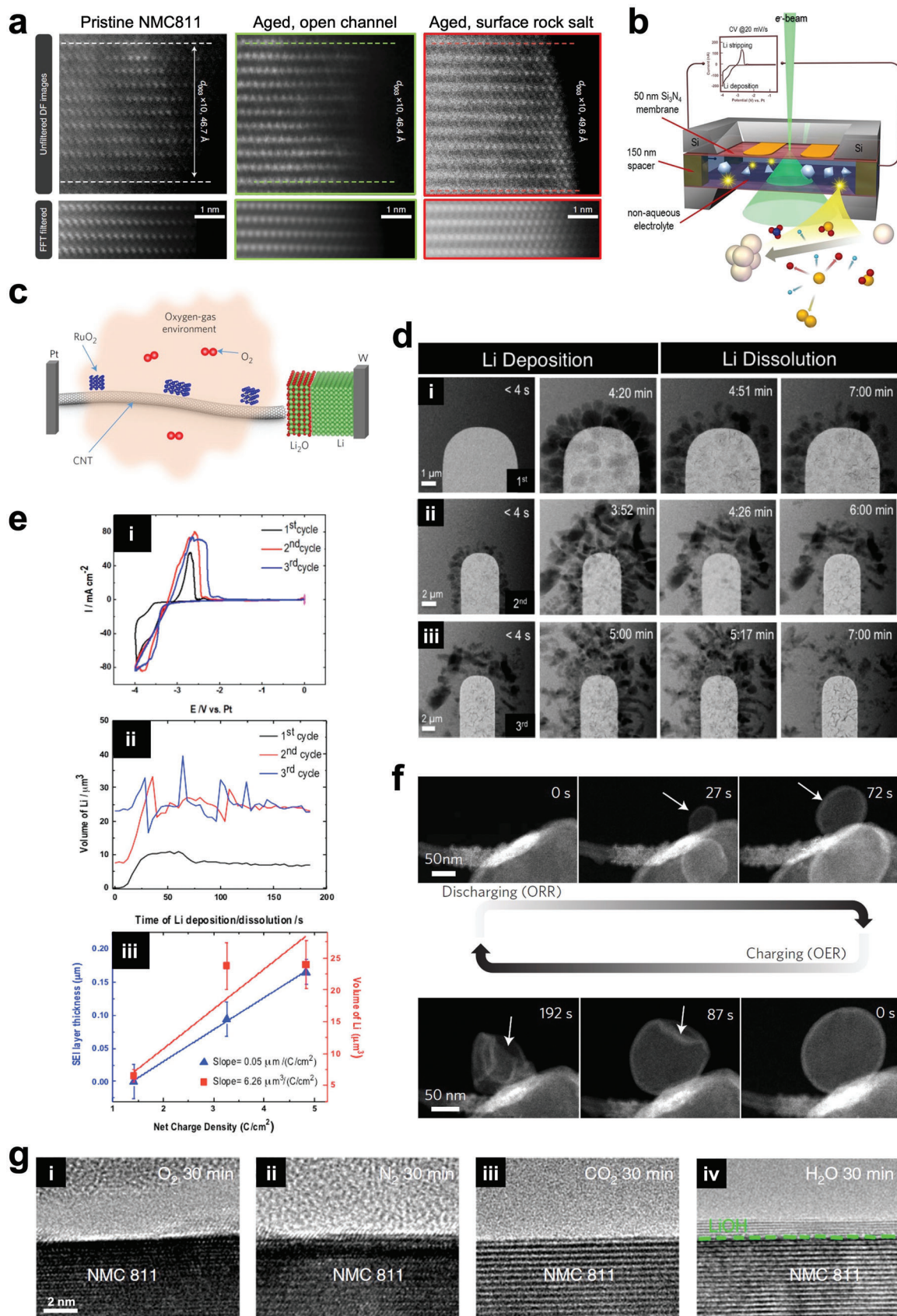
2300103 (9 of 20)

Figure 4. Scanning electron microscopy. a) Zinc dendrite growing shown by FIB-SEM. i–iii) Deposited dendrites, cross-sectional view, 3D reconstruction of single dendrite, and iv) separator torn by dendrites. Reproduced with permission.[105] Copyright 2019, Elsevier. b) Dendrite formation on a K-metal electrode at i,ii) low current density (≈0.5 mA cm^{-2}) and iii,iv) healing with bursts of high current (≈2 mA cm^{-2}). Reproduced with permission.[108] Copyright 2020, NAS. c) Synthesis and characterization of highly nitrated graphene (HNG) -Li$_2$S nanocomposite. i) Schematic illustration showing the preparation of the composite. ii) Low- and high-magnification SEM images of the HNG-L$_2$S$_3$ composite, showing the layer-like Li$_2$S$_3$ coating on HNG. iii) HNG-Li$_2$S composite, showing Li$_2$S islands distribution on HNG. Reproduced with permission.[115] Copyright 2015, Wiley-VCH. d) Comparison of preparing cross-section of commercial Li-metal foil using SEM images and EDS mapping. i,ii) Cross-sectioned and cleaned at room temperature, iii,iv) cross-sectioned at room temperature and cleaned at cryogenic temperature, and v,vi) cross-sectioned and cleaned at cryogenic temperature. Reproduced with permission.[117] Copyright 2019, ACS. e) SEM images display i) dendrite needle at the edge of a Li anode, ii) removed needle by the nanomanipulator, iii) FIB milled dendrite showing hollow morphology, and iv) wall thickness of the dendrite. Reproduced with permission.[112] Copyright 2018, ACS. f) SEM Cross-sections of Li-rich NMC at different cycling stages. Comparison show microscopic damage mechanisms such as internal particle voiding, cracking, exfoliation, and flaking of active material from surface of secondary particles. Reproduced with permission.[121] Copyright 2015, RSC.

ADVANCED
SCIENCE NEWS

www.advancedsciencenews.com

ADVANCED
ENERGY
MATERIALS

www.advenergymat.de

critical thickness and the growth rate is dependent on the nickel (Ni) concentration. Furthermore, the presence of CO_2 can damage the LiOH passivation layer, leading to the formation of discrete islands of Li_2CO_3. Such a passivation layer was found to be self-healed after electron beam damage, and a certain thickness of disordered rock-salt layer can prevent the LiOH layer from growing.

The chemical changes at the electrode/electrolyte interface for all-solid-state batteries have been characterized by in situ STEM coupled with EELS.[139,140] Using a Si|LiPON|LiCoO₂ thin film battery, a disordered interfacial layer (between the white and black dashed lines) forms between the $LiCoO_2$ (LCO) cathode (below the black dashed line) and LiPON electrolyte (above the white dashed line) as shown in **Figure 6**a. As indicated by the low loss EELS with Li K-edge concentration mapping, both the ex situ and in situ sample has more significant integrated intensity in the disordered LCO interfacial layer than that in the pristine sample. Further high loss EELS data shows that Li accumulates and the LCO evolves to rock-salt CoO after cycling.[139]

The in situ and operando TEM cells were used to study the mono- and multivalent ion batteries, including sodium (Na),[141–143] potassium (K),[144] and magnesium (Mg)[145] batteries. Zhu et al.[141] studied the Na ionic transport between different few-layer phosphorene nanosheets by using an in situ open cell. Besides the volume change during Na alloying and dealloying, the Na transport kinetics was found to be dependent on the contact orientation between adjacent nanosheets. The real-time high-resolution TEM and FFT images demonstrate the formation of multiple phases and the stripe-like sodium transport pathway upon Na insertion (Figure 6b). In addition to phosphorene, carbon nanofiber (CNF) was studied for Na plating/stripping by using an in situ open cell.[142] Zeng et al.[143] reported that the Na electrodeposition depends on the surface roughness and SEI thickness, and relatively large Na grains prefer to deposit on the flatter electrode surface by using in situ liquid cell. In situ open cell was used to study the potassiation/depotassiation processes of yolk-shell CNFs coated antimony (Sb@CNFs) electrode materials.[144] HAADF STEM and EDS mapping clearly show the structure of Sb yolk and CNF shell (Figure 6c). Upon in situ cycling, a significant volume change was measured by the in situ open cell (Figure 6d). In situ liquid cell showed that the deposition of hexacoordinated organometallic Mg compounds leads to the irreversible Mg electrodeposition for Mg ion batteries.[145]
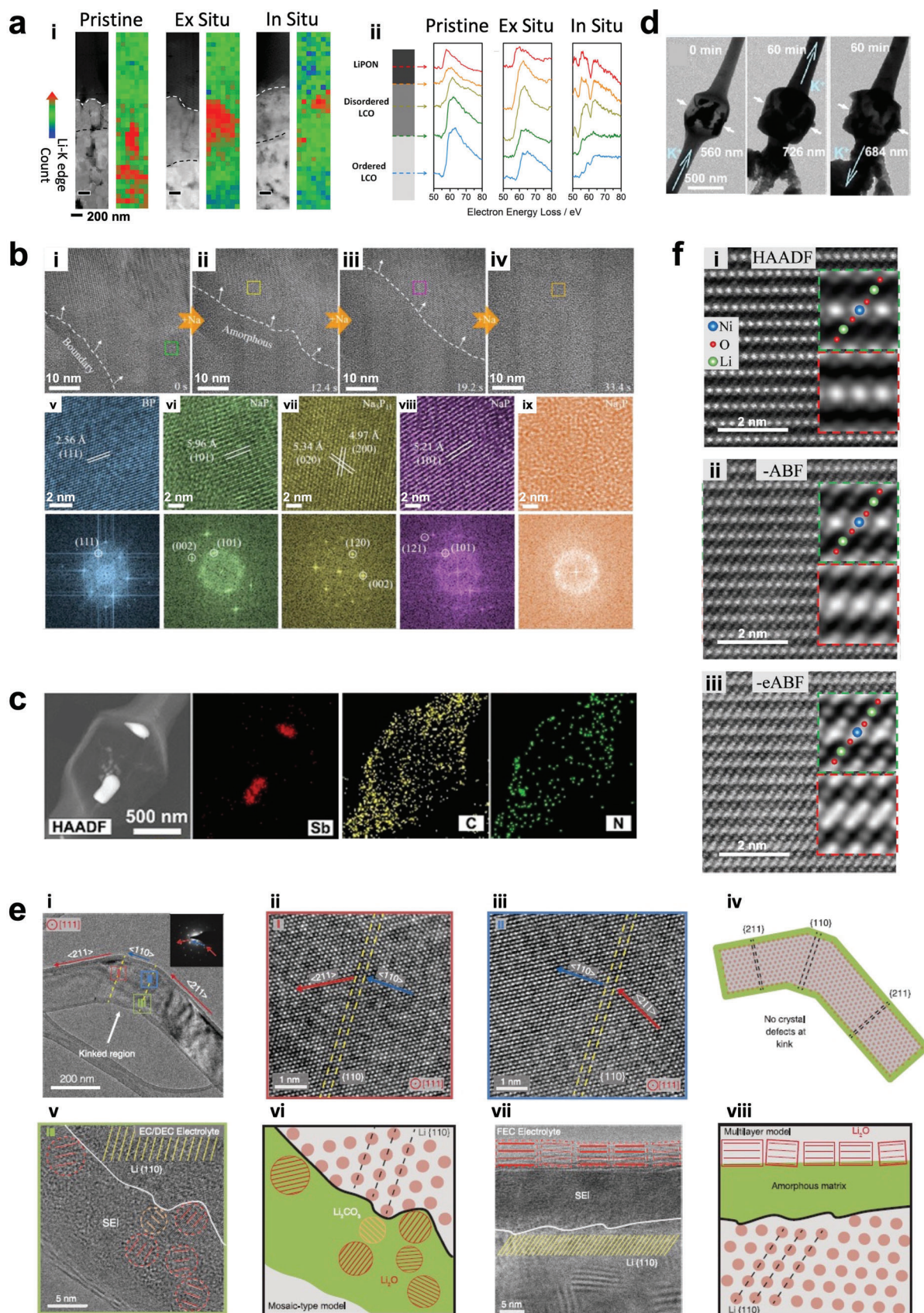
Cyro-TEM is now becoming widely used to image beam-sensitive battery materials.[116,120] Li et al.[116] took the atomic scale TEM image of the Li dendrite. It was found that the growth direction of Li dendrite can change at kinks without any observable crystal defects (Figure 6e). Such defect-free transition could be due to the variation of the SEI composition and/or structure during Li dendrite growth. In addition to the dendrite growth, cyro-TEM provides the direct visualization of SEI (Figure 6e). The widely used carbonate-based electrolyte ethylene carbonate-diethyl carbonate shows a mosaic-type structure, in which inorganic components Li oxide and Li carbonate are dispersed in the amorphous phase. In contrast, a more ordered multilayer-type SEI layer (not shown here) forms for the carbon-based electrolyte with 10 vol% fluoroethylene carbonate. The large grains (≈15 nm) of Li oxide form on top of the amorphous polymer matrix.

Under normal conditions, it is difficult to image battery materials with atomic resolution. For the electrochemically cycled materials, it is even more difficult because of the phase transformation and misorientation. Therefore, 4D-STEM (2D convergent beam electron diffraction patterns at each point in a 2D STEM raster) or ptychography has been used to image light elements, such as Li, in electrode materials.[146,147] By using a pixelated detector, selecting specific angular regions in the diffraction patterns and calculating virtual annular bright-field images, the contrast of the Li atoms in active electrode materials was significantly improved (Figure 6f). The annular bright field (ABF) imaging reveals good sensitivity to Li and O atoms for small specimen thickness. The enhanced ABF was demonstrated to significantly improve the experimental contrast of light elements for larger specimen thicknesses. By using this technique, a gradual transformation from layered to rock-salt phase was observed.

Some future directions are worthy of further study for extensive and deep application of SEM/TEM in battery science and technology. First, beam damage has been a concern especially for the beam-sensitive battery materials or under long-time exposure conditions (e.g., in situ experiments). Subsampling, which is an effective experimental approach for random sparse sampling in STEM and in-painting image reconstruction, has been used to reduce the electron dose/dose-rate, increase the image frame rate, and therefore decrease the beam damage.[148,149] Compressive sensing, which compresses the signal during measurement and accurately recovers it later in software, can be used to increase the frame rate of camera for in situ experiments.[150] Second, new holders are being developed to carry out in situ experiments with multiple external biases and controlled environments. For example, the mechanical properties of Li dendrite was studied by an atomic force microscope—environmental TEM holder.[151,152] Besides, other than the types of batteries mentioned above, more batteries can be studied through ex situ and in situ TEM studies, including but not limited to nickel-, zinc-, aluminum-based batteries, flow batteries, etc.

Figure 5. Transmission electron microscopy. a) High-resolution DF STEM images of pristine NMC811, aged NMC with open Li transport channels, and aged NMC with a rock-salt surface reconstruction layer along the[100] zone axis of the layered rhombohedral R3̄m structure. Reproduced with permission.[125] Copyright 2021, Journal of Materials Chemistry A. b) Schematic of an in situ liquid cell. Reproduced according to the terms of the C-CBY license.[130] Copyright 2016, The authors, published by Springer Nature. c) Schematic of an in situ open and environment cell. Reproduced with permission.[137] Copyright 2017, Nature Nanotechnology. d) i–iii) HAADF STEM images of Li deposition and dissolution cycles at the interface between electrode and electrolyte and e) i) the plots of the CVs, ii) the volume change of Li deposited, and iii) the thickness change of SEI layer for the first three cycles. Reproduced with permission.[131] Copyright 2015, ACS. f) The time-resolved HAADF STEM images illustrating the morphological evolution of the discharge and charge processes for a Li-O₂ nanobattery in an environment open cell. Reproduced with permission.[137] Copyright 2017, Springer Nature. g) HRTEM images showing the delithiation caused by each air component (i–iv) N₂, O₂, CO₂, and water vapor) in the NMC811. Reproduced with permission.[138] Copyright 2020, Springer Nature.

ADVANCED
SCIENCE NEWS

www.advancedsciencenews.com

ADVANCED
ENERGY
MATERIALS

www.advenergymat.de

**ADVANCED
SCIENCE NEWS**

www.advancedsciencenews.com

**ADVANCED
ENERGY
MATERIALS**

www.advenergymat.de

6. Emerging Trends

6.1. Correlative Imaging

In many cases, a single imaging technique is not sufficient to gain a sufficient picture of specific behaviors or connections inside electrodes or battery ensembles (see graphical abstract). Consequently, there is a movement toward coupling several characterization techniques in a correlative workflow, for example, using multiple microscopy techniques to link information across a range of length scales or combining multiple modalities such as imaging, diffraction, and scattering to provide complementary structural, crystallographic, and elemental information.[153] This allows a much richer understanding of damage mechanisms or performance attributes.[153] Furthermore, correlative workflows enable a region of interest (e.g., a defective region) to be identified at a coarse length scale, or identified at one point in time, with one modality (e.g., X-ray CT) to be located and excised (by FIB) for higher resolution imaging or analysis by another (e.g., serial section tomography in the SEM or TEM examination).

Correlative imaging across several length scales from the milli- to the nanometer range has been used to study Li-ion composite electrodes combining non-destructive X-ray micro-/nanoscopy in combination with destructive FIB-SEM imaging in 2 and 3D. Several studies demonstrate that a combination of the techniques can directly characterize the CBD and determine the effective transport properties in different electrode materials including $LiMn_2O_4$ (LMO),[154] NCA,[79] or NMC.[48] Typically, small volumes are selected as a region of interest from 3D X-ray nano CT or physically isolated using FIB-SEM microscopy providing a measurement of porosity which enables the analysis of the diffusivity and tortuosity by segmenting the active material, CBD, and voids. The combination of electron microscopy with X-ray micro-CT allows the determination of a multi-length scale ensemble where the tortuosity factor provides the basis for transport simulations. Moreover, multiscale X-ray CT has been used to detect and quantify defect particles in pristine NMC811 where low resolution imaging presents an overview to improve material statistics, and high resolution reveals crack morphologies.[49,34–36]Multi-modal, correlative imaging can link imaging data with a wide range of secondary characterization tools including acoustic time-of-flight spectroscopy combined with X-ray micro-CT, for studies of internal mechanical deformation and gas-induced degradation in LIBs.[155] Thus, a combination from radiographical imaging with electrochemical impedance spectroscopy allow the quantitative mapping of gas evolution resulting from electrolyte decay as shown from Michalak et al.[39] using neutron radiography and DEMS. Further, the combination of "bulk" and surface sensitive tools can reveal the interparticle ionic transport from Li poor toward Li-rich particles in LFP electrodes using scanning-TXM combined with XANES and X-ray photoemission electron microscopy.[156] More complex studies using multiple advanced characterization techniques such as shown by Xu et al.[125] studying structural driven degradation mechanism during aging of Ni-rich NMC811. Operando synchrotron-XRD in combination with ex situ NMR and STEM and others was used to a new fatigued phase as a function of cycle number. XRD shows the increase of fatigued states during increasing cycling number, ^{7}Li NMR showed the change of local structure and slight Li-ion mobility decrease for aged samples and STEM provided the evidence of structural changes on the crystal surface.

6.2. Computational Imaging and Machine Learning

A key task for many imaging modalities, including CT, MRI, and STEM, is image reconstruction often from noisy or incomplete data. In this respect "compressed sensing" techniques are key, where the aim is to compute a faithful image from as little data as possible. It is crucial when performing 3D or in situ/operando measurements in cases where the phenomena occur over timescales that limit the amount of signal or the number of projections that can be collected, or when low-dose imaging is required to limit damage to beam-sensitive samples. These can lead to artefacts in both X-ray CT and MRI, and in the latter case noise levels may be limiting when imaging certain chemical species such as Li. In such cases one often makes use of the fact that raw images typically have some degree of sparsity and this assumption may be encoded in a variational regularization framework, in which the desired sparsity of the image reconstruction is promoted through the use of a "regularizer" (e.g., "l1," "TV").[157] This model-driven approach, in addition to having "stability" guarantees, is highly versatile and modular, affords full control over data fidelity and is not reliant on the availability of a large reference dataset. Applications include artefact removal in X-ray CT[158] and undersampled MRI[159] and the processing of low-dose STEM.[160]

Using variational approaches, a number of parameters, such as the regularization parameter, may be selected. Instead of choosing these manually, a supervised machine learning (ML) solution known as "bi-level learning" can be used.[161] Using such a scheme one can even learn an optimized sampling strategy to speed up data acquisition in medical MRI[162] and STEM[148,163] (**Figure 7**a). Data-driven approaches to image processing, more generally, have the potential to yield higher-quality reconstructions through adaptivity to the data, but at the possible cost of loss of generalizability and interpretability. Applications of

Figure 6. Transmission electron microscopy. a) HAADF STEM images of i) the all-solid-state nanobattery along with Li K-edge concentration mapping and ii) spectra from various parts of the layers of the pristine, ex situ and in situ samples. Reproduced with permission.[139] Copyright 2016, ACS. b) i–iv) Time-resolved HRTEM images and v–ix) enlarged HRTEM images with the corresponding FFT patterns showing the structural evolution of few-layer phosphorene during interfacial sodium transport. Reproduced with permission.[141] Copyright 2019,Wiley-VCH. c) HAADF STEM and element mapping images of Sb@CNFs and d) time-resolved TEM images showing the Sb@CNFs at the pristine state, after first potassiation and after first depotassiation. Reproduced with permission.[144] Copyright 2020, Wiley-VCH. e) i–iv) TEM images and schematic of the kinked Li metal dendrite that changes from <211> to <110> and back to <211> growth direction. v–viii) TEM images and schematics showing the SEI interfaces with mosaic-type model and multilayer model. Reproduced with permission.[116] Copyright 2017, Science. f) High-resolution HAADF, ABF, and eABF images of LNO viewed along the[100] orientation. The green- and red-bordered insets are averaged experimental and simulated images, respectively. Reproduced with permission.[146] Copyright 2020, Wiley-VCH.
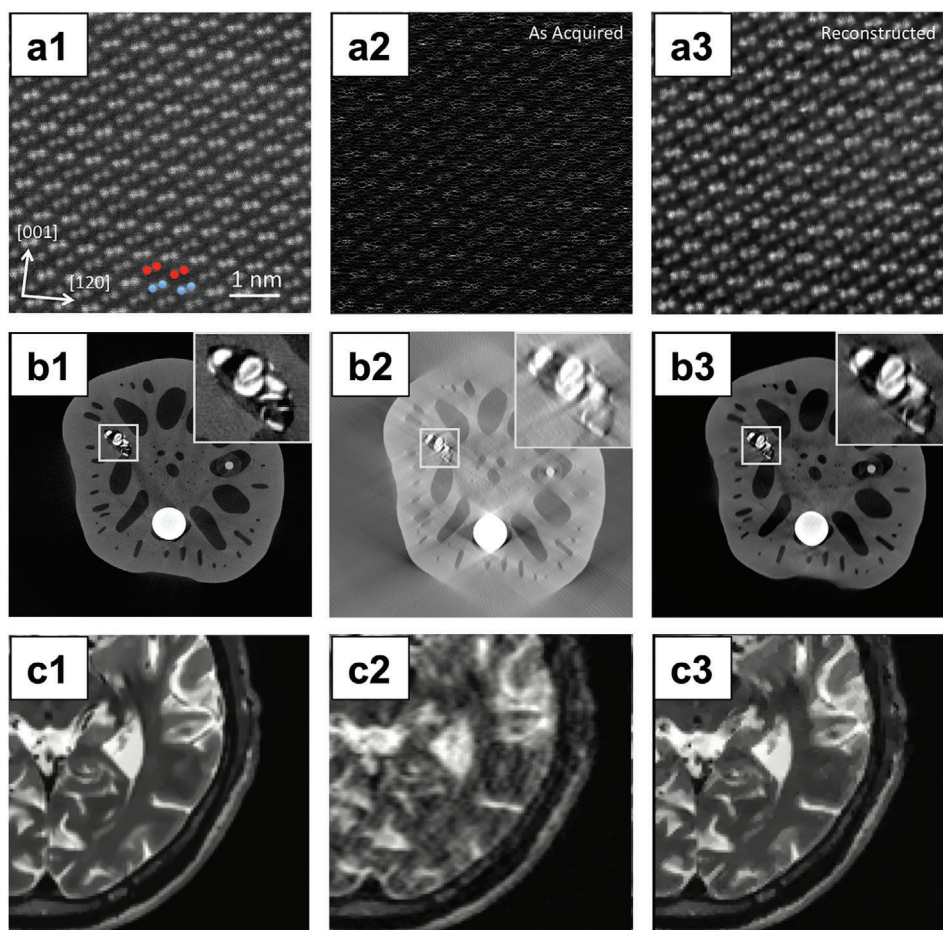
ADVANCED
SCIENCE NEWS

www.advancedsciencenews.com

ADVANCED
ENERGY
MATERIALS

www.advenergymat.de

Figure 7. Reconstructions exploiting machine learning. a) STEM data; a1) fully-sampled STEM image of NITiO$_3$ microstructure, a2) reconstruction from low-dose STEM, a3) reconstruction using a machine-learning method. Reproduced with permission.[148] Copyright 2016, AIP. b) X-ray CT data; b1) image from fully-sampled data, b2) reconstruction from limited-angle data using FBP, b3) reconstruction using machine-learning-based method. Reproduced with permission.[169] Copyright 2019, Inverse Problems. c) MRI data; c1) image from fully-sampled data, c2) reconstruction using Fourier inverse, c3) reconstruction using a guided method. Reproduced with permission.[172] Copyright 2016, SIAM.

deep convolutional neural networks include i) directly learning the mapping from data to reconstructions,[164] ii) unrolled algorithms as NN architectures,[165] and iii) post-processing for artefact removal.[166] Many cutting-edge "hybrid" techniques aim to take the best from both model-driven and data-driven approaches, see ref. [167] for a review. Such techniques have been successfully applied, for instance, to PAT[168] and to limited-angle CT[169,170] (Figure 7b).

Although the above-described frameworks are powerful approaches to single-modality processing, when one has multimodal data, it is of course desirable to exploit their correlations during processing. For example, CT, MRI, and STEM are complementary to one another in the sense that they naturally probe different length-scales and have varying material sensitivity. One could therefore seek a best-of-all-worlds reconstruction by "fusing" images from disparate modalities. In particular, in "guided processing" one aims to exploit a high-quality correlated guide image in the processing of lower-quality target data[171–173] (Figure 7c). We highlight that these techniques can be extended to be robust to mis-registration of the guide and target data, which

is especially pertinent when the data is obtained through multiple experiments of different contrast and resolution and possible artefacts.[174] Related to this is the more difficult problem of "synergistic" reconstruction; that is to say, simultaneous image reconstruction from multi-modality data.[175]

The field of dynamic imaging[176] has promising potential in in situ/operando applications. Here, the rate of the physical processes under investigation imposes strict requirements on the data sampling rate needed, often leading to low-resolution or noisy data. In this case, the data may be more effectively processed by exploiting time-spatial correlations via "low-rank" methods[177] or via temporal models.[178] As a special case of the latter, one can enforce the conformance of the image reconstructions to some fixed physical model, for example, a model for dendrite growth.

Finally, we note that although we have only touched here on image reconstruction, ML techniques have also been successfully applied to relevant problems in data analysis such as the automatic identification of fractures in electrode materials[179] and of dendrites.[180] It is clear that the applications of computational

**ADVANCED
SCIENCE NEWS**

www.advancedsciencenews.com

**ADVANCED
ENERGY
MATERIALS**

www.advenergymat.de

science and ML in battery science (and materials science, more broadly) are manifold and poised for rapid development in coming years. Beyond this, real-time data analysis and ML feedback may even inform acquisition, to maximize the collection of "useful" data, which is particularly important during time-sensitive experiments such as those conducted at particle accelerators.

7. Conclusion and Future Opportunities

We have presented a concise summary of the applications of multi-modal and multi-scale imaging and its application to advanced batteries, as well as perspectives on the growing importance of correlative imaging and ML to provide and combine alternative contrast modes, and to optimize collection protocols to maximize throughput and signal-to-noise ration. Next, we will consider future challenges and opportunities for the field and provide an opinion on the central role of these characterization tools to advancing the progress of energy storage materials, and functional materials more widely.

Batteries, of almost every type, rely on complex porous electrodes to support the electrochemical reactions, electron and ion transport to provide their energy storage capacity; from a microscopist's perspective, they provide almost unparalleled interest in respect of the hierarchy of structure, and the range of materials involved. From nano-scale interfaces,[125] to device level architecture,[34,55] spanning gaseous species from electrolyte decomposition, to low-Z Li metal electrodes, organic anodes, inorganic cathodes, and a range of structural materials.

The microscopy toolbox at the general disposal of the battery community provides unparalleled opportunities for the collection of rich data sets which combine micro-structure, chemistry and crystallography, and the increasing movement toward in situ and operando approaches presents unique insights and challenges, not least in the ability to effectively interpret and analyze the large quantities of available data, and synthesize this into rational design criteria to improve electrode design. More than a decade after the first micron-scale tomographic experiments on battery electrodes, there remains an open question on what constitutes a "good microstructure"? Naturally, there is no universal answer to this, and the design of battery materials is tailored toward application criteria which may favor energy or power density, safety, durability, or cost. Critically, microscopy tools such as those presented here, allow the battery designer to effectively navigate this complex space, and in concert with advanced modelling tools (see, e.g., Xu et al.[181]), to under-take sophisticated multi-parameter optimization.[182]

With the benefit of this toolbox, it is increasingly possible to intelligently iterate potential designs (both experimentally and in silico) such that optimized designs can be more rapidly achieved. This approach is also attractive for the evaluation of novel electrode processing routes, such as directional ice templating,[46,183] magnetic alignment,[184,185] and spray deposition.[186] At the cell manufacturing level, the emerging opportunities for high throughput X-ray tomography provides a compelling opportunity to integrate these tools in metrology and quality control strategies.[187] More widely, the largely "chemistry agnostic" nature of the microscopy and modelling tools presented provides a compelling opportunity to facilitate the commercialization of a host of next generation battery chemistries (LiS, Na-ion, SSB,

etc.). Consequently, their deployment can be accelerated compared with Li-ion and other more traditional chemistries where the more limited suite of contemporary microscopy tools restricted their development to principally empirical means.

Provided that any damage of the sample can be mitigated during acquisition[74,148,149] operando investigations can not only provide a view of the working environment of an operating battery, but also time resolved data describing microstructural evolution; such '4 Dimensional' studies (3D in space + time) are now well established and additional "dimensionality" for example by the addition of chemical or crystallographic information are increasingly commonplace. The opportunity therefore exists not only to understand electrode materials in the "as-designed" state, but also to observe (and ultimately predict) how a given material will evolve. Whilst the microscopy tools provide the means to visualize these changes, tandem developments in algorithms to interpret this "time-lapse" data are required. Moreover, in combination with appropriately designed accelerated stress tests, these advanced microscopy and analysis tools may provide a "crystal ball" to examine how cells respond to varying external stimuli, and afford the battery designer a perspective on cell durability, degradation, and failure. Tensioning the numerous requirements for batteries across a spectrum of applications (cost, lifetime, rate, energy density, safety, etc.) is a widely acknowledged challenge, and on which can be more readily addressed with input from these advanced characterization tools.

Finally, in the context of their growing importance, we should consider the expanding requirements for accessing these tools: the portfolio of microscopy tools considered requires not only extensive capital investment but also extensive expertise spanning instrument development, in situ environments, and advanced analysis. The democratization of access to service the scientific community, alongside parallel developments in sample throughput and automation to service industrial research is required. Examples from the application of advanced microscopy tools in semi-conductor fabrication may serve as useful precedents in this respect.

In conclusion, developments in advanced microscopy tools (and associated analysis) are continuing at pace, and the energy storage community is well equipped with a toolbox to improve fundamental understanding of materials properties, and to enhance design and optimization of materials and devices. Trends toward correlative microscopy are paying dividends in the rich information now obtainable which span length scales and myriad probes and contrast generation mechanisms. Similarly, the ability to undertake time-lapse and operando imaging increasingly extends investigations into the time domain, where multi-dimensional imaging is poised to make substantial contributions to the development and deployment of next generation materials spanning a host of disciplines, not limited to energy storage, but spanning a range of fields including catalytic and functional materials, bio-materials, additive manufacturing, metallurgy, and corrosion.

Acknowledgements

Conflict of Interest

The authors declare no conflict of interest.

Author Contributions

R.F.Z., T.M.M.H., and P.R.S. conceived and designed the study. P.K. and M.M.B. mainly contributed to the MRI/EPRI section. R.F.Z. mainly contributed to the neutron imaging and correlative imaging section. T.M.M.H. and I.R. mainly contributed to the X-ray imaging section. W.L., M.E.C., L.B.M., and N.D.B. mainly contributed to the EM section. J.W. and M.J.E. mainly contributed to the ML section. P.R.S. mainly contributed to the Introduction and Future opportunities/Discussion section. T.L.B., D.J.L.B., P.Q., and P.J.W. contributed to the writing and reviewing of the final paper.

Keywords

correlative microscopy, in situ imaging, Li-ion batteries, microscopy, multidimensional characterization, time-resolved

[1] M. M. Britton, *Prog. Nucl. Magn. Reson. Spectrosc.* **2017**, *101*, 51.

[2] M. M. Britton, *ChemPhysChem* **2014**, *15*, 1731.

[3] O. Pecher, J. Carretero-Gonzalez, K. J. Griffith, C. P. Grey, *Chem. Mater.* **2017**, *29*, 213.

[4] M. M. Britton, P. M. Bayley, P. C. Howlett, A. J. Davenport, M. Forsyth, *J. Phys. Chem. Lett.* **2013**, *4*, 3019.

[5] J. M. Bray, C. L. Doswell, G. E. Pavlovskaya, L. Chen, B. Kishore, H. Au, H. Alptekin, E. Kendrick, M. M. Titirici, T. Meersmann, M. M. Britton, *Nat. Commun.* **2020**, *11*, 2083.

[6] S. A. Krachkovskiy, J. D. Bazak, P. Werhun, B. J. Balcom, I. C. Halalay, G. R. Goward, *J. Am. Chem. Soc.* **2016**, *138*, 7992.

[7] C. P. Grey, J. M. Tarascon, *Nat. Mater.* **2016**, *16*, 45.

[8] H. J. Chang, A. J. Ilott, N. M. Trease, M. Mohammadi, A. Jerschow, C. P. Grey, *J. Am. Chem. Soc.* **2015**, *137*, 15209.

[9] H. J. Chang, N. M. Trease, A. J. Ilott, D. Zeng, L. S. Du, A. Jerschow, C. P. Grey, *J. Phys. Chem. C* **2015**, *119*, 16443.

[10] S. Chandrashekar, N. M. Trease, H. J. Chang, L.-S. Du, C. P. Grey, A. Jerschow, *Nat. Mater.* **2012**, *11*, 311.

[11] M. Klett, M. Giesecke, A. Nyman, F. Hallberg, R. W. Lindström, G. Lindbergh, I. Furó, *J. Am. Chem. Soc.* **2012**, *134*, 14654.

[12] Y. Xiang, G. Zheng, Z. Liang, Y. Jin, X. Liu, S. Chen, K. Zhou, J. Zhu, M. Lin, H. He, J. Wan, S. Yu, G. Zhong, R. Fu, Y. Li, Y. Yang, *Nat. Nanotechnol.* **2020**, *15*, 883.

[13] A. K. Sethurajan, S. A. Krachkovskiy, I. C. Halalay, G. R. Goward, B. Protas, *J. Phys. Chem. B* **2015**, *119*, 12238.

[14] A. J. Ilott, M. Mohammadi, H. J. Chang, C. P. Grey, A. Jerschow, *Proc. Natl. Acad. Sci. U. S. A.* **2016**, *113*, 10779.

[15] A. J. Ilott, M. Mohammadi, C. M. Schauerman, M. J. Ganter, A. Jerschow, *Nat. Commun.* **2018**, *9*, 1776.

[16] M. A. Hope, B. L. D. Rinkel, A. B. Gunnarsdóttir, K. Märker, S. Menkin, S. Paul, I. V. Sergeyev, C. P. Grey, *Nat. Commun.* **2020**, *11*, 2224.

[17] M. Sathiya, J. B. Leriche, E. Salager, D. Gourier, J. M. Tarascon, H. Vezin, *Nat. Commun.* **2015**, *6*, 6276.

[18] A. Niemöller, P. Jakes, S. Eurich, A. Paulus, H. Kungl, R. A. Eichel, J. Granwehr, *J. Chem. Phys.* **2018**, *148*, 014705.

[19] A. Niemöller, P. Jakes, R. A. Eichel, J. Granwehr, *Sci. Rep.* **2018**, *8*, 14331.

[20] F. Geng, Q. Yang, C. Li, M. Shen, Q. Chen, B. Hu, *Chem. Mater.* **2021**, *33*, 8223.

[21] C.-E. Dutoit, M. Tang, D. Gourier, J.-M. Tarascon, H. Vezin, E. Salager, *Nat. Commun.* **2021**, *12*, 1410.

[22] R. H. Taylor, *Adv. Phys.* **1975**, *24*, 681.

[23] M. Kamata, T. Esaka, N. Kodama, S. Fujine, K. Yoneda, K. Kanda, *J. Electrochem. Soc.* **1996**, *143*, 1866.

[24] S. Takai, T. Mandai, Y. Kawabata, T. Esaka, *Solid State Ionics* **2005**, *176*, 2227.

[25] R. F. Ziesche, N. Kardjilov, W. Kockelmann, D. J. L. Brett, P. R. Shearing, *Joule* **2022**, *6*, 35.

[26] J. B. Siegel, A. G. Stefanopoulou, P. Hagans, Y. Ding, D. Gorsich, *J. Electrochem. Soc.* **2013**, *160*, A1031.

[27] J. B. Siegel, X. Lin, A. G. Stefanopoulou, D. S. Hussey, D. L. Jacobson, D. Gorsich, *J. Electrochem. Soc.* **2011**, *158*, A523.

[28] J. P. Owejan, J. J. Gagliardo, S. J. Harris, H. Wang, D. S. Hussey, D. L. Jacobson, *Electrochim. Acta* **2012**, *66*, 94.

[29] Z. Nie, S. Ong, D. S. Hussey, J. M. LaManna, D. L. Jacobson, G. M. Koenig, *Mol. Syst. Des. Eng.* **2020**, *5*, 245.

[30] P. J. Withers, C. Bouman, S. Carmignato, V. Cnudde, D. Grimaldi, C. K. Hagen, E. Maire, M. Manley, A. Du Plessis, S. R. Stock, *Nat. Rev. Methods Primers* **2021**, *1*, 21.

[31] B. Song, I. Dhiman, J. C. Carothers, G. M. Veith, J. Liu, H. Z. Bilheux, A. Huq, *ACS Energy Lett.* **2019**, *4*, 2402.

[32] Y. Zhang, K. S. R. Chandran, H. Z. Bilheux, *J. Power Sources* **2018**, *376*, 125.

[33] J. Nanda, H. Bilheux, S. Voisin, G. M. Veith, R. Archibald, L. Walker, S. Allu, N. J. Dudney, S. Pannala, *J. Phys. Chem. C* **2012**, *116*, 8401.

[34] R. F. Ziesche, T. Arlt, D. P. Finegan, T. M. M. Heenan, A. Tengattini, D. Baum, N. Kardjilov, H. Markötter, I. Manke, W. Kockelmann, D. J. L. Brett, P. R. Shearing, *Nat. Commun.* **2020**, *11*, 777.

[35] R. F. Ziesche, J. B. Robinson, M. D. R. Kok, H. Markötter, W. Kockelmann, N. Kardjilov, I. Manke, D. J. L. Brett, P. R. Shearing, *J. Electrochem. Soc.* **2020**, *167*, 130545.

[36] R. F. Ziesche, J. B. Robinson, H. Markötter, R. Bradbury, A. Tengattini, N. Lenoir, L. Helfen, W. Kockelmann, N. Kardjilov, I. Manke, D. J. L. Brett, P. R. Shearing, *J. Electrochem. Soc.* **2020**, *167*, 140509.

[37] D. Goers, M. Holzapfel, W. Scheifele, E. Lehmann, P. Vontobel, P. Novák, *J. Power Sources* **2004**, *130*, 221.

[38] B. Michalak, H. Sommer, D. Mannes, A. Kaestner, T. Brezesinski, J. Janek, *Sci. Rep.* **2015**, *5*, 15627.

[39] B. Michalak, B. B. Berkes, H. Sommer, T. Bergfeldt, T. Brezesinski, J. Janek, *Anal. Chem.* **2016**, *88*, 2877.

[40] B. Starke, S. Seidlmayer, M. Schulz, A. Dinter, Z. Revay, R. Gilles, K.-H. Pettinger, *J. Electrochem. Soc.* **2017**, *164*, A3943.

[41] I. Manke, J. Banhart, A. Haibel, A. Rack, S. Zabler, N. Kardjilov, A. Hilger, A. Melzer, H. Riesemeier, *Appl. Phys. Lett.* **2007**, *90*, 214102.

[42] J. B. Habedank, F. J. Günter, N. Billot, R. Gilles, T. Neuwirth, G. Reinhart, M. F. Zaeh, *Int. J. Adv. Manuf. Technol.* **2019**, *102*, 2769.

[43] A. Senyshyn, M. J. Mühlbauer, O. Dolotko, M. Hofmann, H. Ehrenberg, *Sci. Rep.* **2016**, *5*, 18380.

[44] E. Ametova, G. Burca, S. Chilingaryan, G. Fardell, J. S. Jrgensen, E. Papoutsellis, E. Pasca, R. Warr, M. Turner, W. R. B. Lionheart, P. J. Withers, *J. Phys. D: Appl. Phys.* **2021**, *54*, 325502.

[45] T. Kamiyama, Y. Narita, H. Sato, Y. Ohnuma, Y. Kiyanagi, *Phys. Procedia* **2017**, *88*, 27.

[46] R. F. Ziesche, A. S. Tremsin, C. Huang, C. Tan, P. S. Grant, M. Storm, D. J. L. Brett, P. R. Shearing, W. Kockelmann, *J. Imaging* **2020**, *6*, 136.

[47] E. Maire, P. J. Withers, *Int. Mater. Rev.* **2014**, *59*, 1.

[48] S. R. Daemi, C. Tan, T. Volkenandt, S. J. Cooper, A. Palacios-Padros, J. Cookson, D. J. L. Brett, P. R. Shearing, *ACS Appl. Energy Mater.* **2018**, *1*, 3702.

[49] T. M. M. Heenan, A. Wade, C. Tan, J. E. Parker, D. Matras, A. S. Leach, J. B. Robinson, A. Llewellyn, A. Dimitrijevic, R. Jervis, P. D. Quinn, D. J. L. Brett, P. R. Shearing, *Adv. Energy Mater.* **2020**, *10*, 2002655.

[50] D. P. Finegan, E. Darcy, M. Keyser, B. Tjaden, T. M. M. Heenan, R. Jervis, J. J. Bailey, R. Malik, N. T. Vo, O. V. Magdysyuk, R. Atwood, M. Drakopoulos, M. DiMichiel, A. Rack, G. Hinds, D. J. L. Brett, P. R. Shearing, *Energy Environ. Sci.* **2017**, *10*, 1377.

[51] F. Larsson, P. Andersson, B. E. Mellander, *Batteries* **2016**, *2*, 9.

[52] J. Robinson, D. Finegan, T. Heenan, K. Smith, E. Kendrick, D. Brett, P. R. Shearing, *J. Electrochem. Energy Convers. Storage* **2017**, *15*, 011010.

[53] V. Yufit, P. Shearing, R. W. Hamilton, P. D. Lee, M. Wu, N. P. Brandon, *Electrochem. Commun.* **2011**, *13*, 608.

[54] T. Yokoshima, D. Mukoyama, F. Maeda, T. Osaka, K. Takazawa, S. Egusa, S. Naoi, S. Ishikura, K. Yamamoto, *J. Power Sources* **2018**, *393*, 67.

[55] M. D. R. Kok, J. B. Robinson, J. S. Weaving, A. Jnawali, M. Pham, F. Iacoviello, D. J. L. Brett, P. R. Shearing, *Sustainable Energy Fuels* **2019**, *3*, 2972.

[56] A. Ran, S. Chen, S. Zhang, S. Liu, Z. Zhou, P. Nie, K. Qian, L. Fang, S. X. Zhao, B. Li, F. Kang, X. Zhou, H. Sun, X. Zhang, G. Wei, *RSC Adv.* **2020**, *10*, 19117.

[57] D. P. Finegan, M. Scheel, J. B. Robinson, B. Tjaden, I. Hunt, T. J. Mason, J. Millichamp, M. Di Michiel, G. J. Offer, G. Hinds, D. J. L. Brett, P. R. Shearing, *Nat. Commun.* **2015**, *6*, 6924.

[58] P. R. Shearing, L. E. Howard, P. S. Jørgensen, N. P. Brandon, S. J. Harris, *Electrochem. Commun.* **2010**, *12*, 374.

[59] S. Müller, J. Eller, M. Ebner, C. Burns, J. Dahn, V. Wood, *J. Electrochem. Soc.* **2018**, *165*, A339.

[60] Y. C. K. Chen-Wiegart, P. Shearing, Q. Yuan, A. Tkachuk, J. Wang, *Electrochem. Commun.* **2012**, *21*, 58.

[61] M. Ebner, F. Marone, M. Stampanoni, V. Wood, *Science* **2013**, *342*, 716.

[62] Z. Liu, J. S. Cronin, Y. C. K. Chen-Wiegart, J. R. Wilson, K. J. Yakal-Kremski, J. Wang, K. T. Faber, S. A. Barnett, *J. Power Sources* **2013**, *227*, 267.

[63] P.-C. Tsai, B. Wen, M. Wolfman, M.-J. Choe, M. S. Pan, L. Su, K. Thornton, J. Cabana, Y.-M. Chiang, *Energy Environ. Sci.* **2018**, *11*, 860.

[64] T. M. M. Heenan, A. V. Llewellyn, A. S. Leach, M. D. R. Kok, C. Tan, R. Jervis, D. J. L. Brett, P. R. Shearing, *Adv. Sci.* **2020**, *7*, 2000362.

[65] B. Bozzini, C. Mele, A. Veneziano, N. Sodini, G. Lanzafame, A. Taurino, L. Mancini, *ACS Appl. Energy Mater.* **2020**, *3*, 4931.

[66] R. Xu, J. Xiang, J. Feng, X. Lu, Z. Hao, L. Kang, M. Li, Y. Wu, C. Tan, Y. Liu, G. He, D. J. L. Brett, P. R. Shearing, L. Yuan, Y. Huang, F. R. Wang, *Energy Storage Mater.* **2020**, *31*, 164.

[67] C. Villevieille, M. Ebner, J. L. Gómez-Cámer, F. Marone, P. Novák, V. Wood, *Adv. Mater.* **2015**, *27*, 1676.

[68] O. O. Taiwo, T. M. M. Heenan, D. P. Finegan, D. J. L. Brett, P. R. Shearing, J. M. Paz-García, S. A. Hall, R. Mokso, P. Villanueva-Pérez, A. Patera, *J. Power Sources* **2017**, *342*, 904.

[69] P. Pietsch, D. Westhoff, J. Feinauer, J. Eller, F. Marone, M. Stampanoni, V. Schmidt, V. Wood, *Nat. Commun.* **2016**, *7*, 12909.

[70] D. S. Eastwood, P. M. Bayley, H. J. Chang, O. O. Taiwo, J. Vila-Comamala, D. J. L. Brett, C. Rau, P. J. Withers, P. R. Shearing, C. P. Grey, P. D. Lee, *Chem. Commun.* **2015**, *51*, 266.

[71] S. Hao, S. R. Daemi, T. M. M. Heenan, W. Du, C. Tan, M. Storm, C. Rau, D. J. L. Brett, P. R. Shearing, *Nano Energy* **2021**, *82*, 105744.

[72] B. S. Vishnugopi, M. B. Dixit, F. Hao, B. Shyam, J. B. Cook, K. B. Hatzell, P. P. Mukherjee, *Adv. Energy Mater.* **2022**, *12*, 2102825.

[73] J. A. Lewis, F. J. Q. Cortes, Y. Liu, J. C. Miers, A. Verma, B. S. Vishnugopi, J. Tippens, D. Prakash, T. S. Marchese, S. Y. Han, C. Lee, P. P. Shetty, H. W. Lee, P. Shevchenko, F. De Carlo, C. Saldana, P. P. Mukherjee, M. T. McDowell, *Nat. Mater.* **2021**, *20*, 503.

[74] C. Lim, H. Kang, V. De Andrade, F. De Carlo, L. Zhu, *J. Synchrotron Radiat.* **2017**, *24*, 695.

[75] D. P. Finegan, S. J. Cooper, B. Tjaden, O. O. Taiwo, J. Gelb, G. Hinds, D. J. L. Brett, P. R. Shearing, *J. Power Sources* **2016**, *333*, 184.

[76] C. Rahe, S. T. Kelly, M. N. Rad, D. U. Sauer, J. Mayer, E. Figgemeier, *J. Power Sources* **2019**, *433*, 126631.

[77] T. M. M. Heenan, A. Jnawali, M. D. R. Kok, T. G. Tranter, C. Tan, A. Dimitrijevic, R. Jervis, D. J. L. Brett, P. R. Shearing, *J. Electrochem. Soc.* **2020**, *167*, 140530.

[78] P. R. Shearing, N. P. Brandon, J. Gelb, R. Bradley, P. J. Withers, A. J. Marquis, S. Cooper, S. J. Harris, *J. Electrochem. Soc.* **2012**, *159*, A1023.

[79] J. Gelb, D. P. Finegan, D. J. L. Brett, P. R. Shearing, *J. Power Sources* **2017**, *357*, 77.

[80] C. Tan, S. Daemi, T. Heenan, F. Iacoviello, A. S. Leach, L. Rasha, R. Jervis, D. J. L. Brett, P. R. Shearing, *J. Electrochem. Soc.* **2020**, *167*, 060512.

[81] J. J. Bailey, T. M. M. Heenan, D. P. Finegan, X. Lu, S. R. Daemi, F. Iacoviello, N. R. Backeberg, O. O. Taiwo, D. J. L. Brett, A. Atkinson, P. R. Shearing, *J. Microsc.* **2017**, *267*, 384.

[82] M. Ebner, D. W. Chung, R. E. García, V. Wood, *Adv. Energy Mater.* **2014**, *4*, 1301278.

[83] X. Lu, A. Bertei, D. P. Finegan, C. Tan, S. R. Daemi, J. S. Weaving, K. B. O'Regan, T. M. M. Heenan, G. Hinds, E. Kendrick, D. J. L. Brett, P. R. Shearing, *Nat. Commun.* **2020**, *11*, 2079.

[84] F. L. E. Usseglio-Viretta, A. Colclasure, A. N. Mistry, K. P. Y. Claver, F. Pouraghajan, D. P. Finegan, T. M. M. Heenan, D. Abraham, P. P. Mukherjee, D. Wheeler, P. Shearing, S. J. Cooper, K. Smith, *J. Electrochem. Soc.* **2018**, *165*, A3403.

[85] T. G. Tranter, R. Timms, T. M. M. Heenan, S. G. Marquis, V. Sulzer, A. Jnawali, M. D. R. Kok, C. P. Please, S. J. Chapman, P. R. Shearing, D. J. L. Brett, *J. Electrochem. Soc.* **2020**, *167*, 110538.

[86] Z. A. Khan, P. A. G. Salaberri, T. M. M. Heenan, R. Jervis, P. R. Shearing, D. Brett, A. Elkamel, J. T. Gostick, *J. Electrochem. Soc.* **2020**, *167*, 040528.

[87] Z. Su, V. De Andrade, S. Cretu, Y. Yin, M. J. Wojcik, A. A. Franco, A. Demortière, *ACS Appl. Energy Mater.* **2020**, *3*, 4093.

[88] E. H. R. Tsai, J. Billaud, D. F. Sanchez, J. Ihli, M. Odstrčil, M. Holler, D. Grolimund, C. Villevieille, M. Guizar-Sicairos, *iScience* **2019**, *11*, 356.

[89] L. R. Brandt, J. J. Marie, T. Moxham, D. P. Förstermann, E. Salvati, C. Besnard, C. Papadaki, Z. Wang, P. G. Bruce, A. M. Korsunsky, *Energy Environ. Sci.* **2020**, *13*, 3556.

[90] Z. Xu, Z. Jiang, C. Kuai, R. Xu, C. Qin, Y. Zhang, M. M. Rahman, C. Wei, D. Nordlund, C.-J. Sun, X. Xiao, X.-W. Du, K. Zhao, P. Yan, Y. Liu, F. Lin, *Nat. Commun.* **2020**, *11*, 83.

[91] A. Ulvestad, A. Singer, J. N. Clark, H. M. Cho, J. W. Kim, R. Harder, J. Maser, Y. S. Meng, O. G. Shpyrko, *Science* **2015**, *348*, 1344.

[92] A. Singer, M. Zhang, S. Hy, D. Cela, C. Fang, T. A. Wynn, B. Qiu, Y. Xia, Z. Liu, A. Ulvestad, N. Hua, J. Wingert, H. Liu, M. Sprung, A. V. Zozulya, E. Maxey, R. Harder, Y. S. Meng, O. G. Shpyrko, *Nat. Energy* **2018**, *3*, 641.

[93] A. K. C. Estandarte, J. Diao, A. V. Llewellyn, A. Jnawali, T. M. M. Heenan, S. R. Daemi, J. J. Bailey, S. Cipiccia, D. Batey, X. Shi, C. Rau, D. J. L. Brett, R. Jervis, I. K. Robinson, P. R. Shearing, *ACS Nano* **2021**, *15*, 1321.

[94] D. P. Finegan, A. Vamvakeros, C. Tan, T. M. M. Heenan, S. R. Daemi, N. Seitzman, M. Di Michiel, S. Jacques, A. M. Beale, D. J. L. Brett, P. R. Shearing, K. Smith, *Nat. Commun.* **2020**, *11*, 631.

[95] G. Tonin, G. B. M. Vaughan, R. Bouchet, F. Alloin, M. Di Michiel, C. Barchasz, *J. Power Sources* **2020**, *468*, 228287.

[96] D. P. Finegan, A. Vamvakeros, L. Cao, C. Tan, T. M. M. Heenan, S. R. Daemi, S. D. M. Jacques, A. M. Beale, M. Di Michiel, K. Smith, D. J. L. Brett, P. R. Shearing, C. Ban, *Nano Lett.* **2019**, *19*, 3811.

[97] S. R. Daemi, C. Tan, A. Vamvakeros, T. M. M. Heenan, D. P. Finegan, M. Di Michiel, A. M. Beale, J. Cookson, E. Petrucco, J. S. Weaving, S. Jacques, R. Jervis, D. J. L. Brett, P. R. Shearing, *Phys. Chem. Chem. Phys.* **2020**, *22*, 17814.

[98] P. J. Goodhew, J. Humphreys, R. Beanland, *Electron Microscopy and Analysis*, CRC Press, Boca Raton **2000**.

[99] K. D. Vernon-Parry, *III-Vs Rev.* **2000**, *13*, 40.

[100] D. B. Williams, C. B. Carter, Transmission Electron Microscopy, Springer-US Boston MA **2009**.

[101] C. A. Volkert, A. M. Minor, *MRS Bull.* **2007**, *32*, 389.

[102] M. D. Uchic, M. A. Groeber, A. D. Rollett, *Jom* **2011**, *63*, 25.

[103] T. L. Burnett, R. Kelley, B. Winiarski, L. Contreras, M. Daly, A. Gholinia, M. G. Burke, P. J. Withers, *Ultramicroscopy* **2016**, *161*, 119.

[104] M. P. Echlin, T. L. Burnett, A. T. Polonsky, T. M. Pollock, P. J. Withers, *Curr. Opin. Solid State Mater. Sci.* **2020**, *24*, 100817.

[105] V. Yufit, F. Tariq, D. S. Eastwood, M. Biton, B. Wu, P. D. Lee, N. P. Brandon, *Joule* **2019**, *3*, 485.

[106] Q. Yang, Q. Li, Z. Liu, D. Wang, Y. Guo, X. Li, Y. Tang, H. Li, B. Dong, C. Zhi, *Adv. Mater.* **2020**, *32*, 2001854.

[107] T. Foroozan, S. Sharifi-Asl, R. Shahbazian-Yassar, *J. Power Sources* **2020**, *461*, 228135.

[108] P. Hundekar, S. Basu, X. Fan, L. Li, A. Yoshimura, T. Gupta, V. Sarbada, A. Lakhnot, R. Jain, S. Narayanan, Y. Shi, C. Wang, N. Koratkar, *Stem Cells Int.* **2020**, *117*, 5588.

[109] H. Chen, H. Xu, B. Zheng, S. Wang, T. Huang, F. Guo, W. Gao, C. Gao, *ACS Appl. Mater. Interfaces* **2017**, *9*, 22628.

[110] F. Wan, L. Zhang, X. Dai, X. Wang, Z. Niu, J. Chen, *Nat. Commun.* **2018**, *9*, 1656.

[111] M. Golozar, A. Paolella, H. Demers, S. Bessette, M. Lagacé, P. Bouchard, A. Guerfi, R. Gauvin, K. Zaghib, *Commun. Chem.* **2019**, *2*, 131.

[112] M. Golozar, P. Hovington, A. Paolella, S. Bessette, M. Lagacé, P. Bouchard, H. Demers, R. Gauvin, K. Zaghib, *Nano Lett.* **2018**, *18*, 7583.

[113] D. Chen, S. Indris, M. Schulz, B. Gamer, R. Mönig, *J. Power Sources* **2011**, *196*, 6382.

[114] G. Rong, X. Zhang, W. Zhao, Y. Qiu, M. Liu, F. Ye, Y. Xu, J. Chen, Y. Hou, W. Li, W. Duan, Y. Zhang, *Adv. Mater.* **2017**, *29*, 1606187.

[115] Y. Qiu, G. Rong, J. Yang, G. Li, S. Ma, X. Wang, Z. Pan, Y. Hou, M. Liu, F. Ye, W. Li, Z. W. Seh, X. Tao, H. Yao, N. Liu, R. Zhang, G. Zhou, J. Wang, S. Fan, Y. Cui, Y. Zhang, *Adv. Energy Mater.* **2015**, *5*, 1501369.

[116] Y. Li, Y. Li, A. Pei, K. Yan, Y. Sun, C.-L. Wu, L.-M. Joubert, R. Chin, A. L. Koh, Y. Yu, J. Perrino, B. Butz, S. Chu, Y. Cui, *Science* **2017**, *358*, 506.

[117] J. Z. Lee, T. A. Wynn, M. A. Schroeder, J. Alvarado, X. Wang, K. Xu, Y. S. Meng, *ACS Energy Lett.* **2019**, *4*, 489.

[118] M. J. Zachman, Z. Tu, L. A. Archer, L. F. Kourkoutis, *ACS Energy Lett.* **2020**, *5*, 1224.

[119] M. Biton, F. Tariq, V. Yufit, Z. Chen, N. Brandon, *Acta Mater.* **2017**, *141*, 39.

[120] M. J. Zachman, Z. Tu, S. Choudhury, L. A. Archer, L. F. Kourkoutis, *Nature* **2018**, *560*, 345.

[121] B. Song, T. Sui, S. Ying, L. Li, L. Lu, A. M. Korsunsky, *J. Mater. Chem. A* **2015**, *3*, 18171.

[122] A. T. Polonsky, M. P. Echlin, W. C. Lenthe, R. R. Dehoff, M. M. Kirka, T. M. Pollock, *Mater. Charact.* **2018**, *143*, 171.

[123] K. Jungjohann, D. Long, R. Gannon, S. Randolph, S. Goriparti, L. Merrill, K. Harrison, *Microsc. Microanal.* **2020**, *26*, 1652.

[124] T. L. Burnett, S. A. McDonald, A. Gholinia, R. Geurts, M. Janus, T. Slater, S. J. Haigh, C. Ornek, F. Almuaili, D. L. Engelberg, G. E. Thompson, P. J. Withers, *Sci. Rep.* **2014**, *4*, 4711.

[125] C. Xu, K. Märker, J. Lee, A. Mahadevegowda, P. J. Reeves, S. J. Day, M. F. Groh, S. P. Emge, C. Ducati, B. L. Mehdi, C. C. Tang, C. P. Grey, *Nat. Mater.* **2021**, *20*, 84.

[126] M. Morcrette, P. Rozier, L. Dupont, E. Mugnier, L. Sannier, J. Galy, J. M. Tarascon, *Nat. Mater.* **2003**, *2*, 755.

[127] P. Poizot, S. Laruelle, S. Grugeon, L. Dupont, J. Tarascon, **Nature** **2000**, 407, 496.

[128] Y. Oumellal, A. Rougier, G. A. Nazri, J. M. Tarascon, L. Aymard, *Nat. Mater.* **2008**, *7*, 916.

[129] P. Abellan, B. L. Mehdi, L. R. Parent, M. Gu, C. Park, W. Xu, Y. Zhang, I. Arslan, J. G. Zhang, C. M. Wang, J. E. Evans, N. D. Browning, *Nano Lett.* **2014**, *14*, 1293.

[130] B. L. Mehdi, A. Stevens, J. Qian, C. Park, W. Xu, W. A. Henderson, J.-G. Zhang, K. T. Mueller, N. D. Browning, *Sci. Rep.* **2016**, *6*, 34267.

[131] B. L. Mehdi, J. Qian, E. Nasybulin, C. Park, D. A. Welch, R. Faller, H. Mehta, W. A. Henderson, W. Xu, C. M. Wang, J. E. Evans, J. Liu, J. G. Zhang, K. T. Mueller, N. D. Browning, *Nano Lett.* **2015**, *15*, 2168.

[132] A. J. Leenheer, K. L. Jungjohann, K. R. Zavadil, J. P. Sullivan, C. T. Harris, *ACS Nano* **2015**, *9*, 4379.

[133] J. Y. Huang, L. Zhong, C. M. Wang, J. P. Sullivan, W. Xu, L. Q. Zhang, S. X. Mao, N. S. Hudak, X. H. Liu, A. Subramanian, H. Fan, L. Qi, A. Kushima, J. Li, *Science* **2010**, *330*, 1515.

[134] M. T. McDowell, Z. Lu, K. J. Koski, J. H. Yu, G. Zheng, Y. Cui, *Nano Lett.* **2015**, *15*, 1264.

[135] W. Li, K. Cao, H. Wang, J. Liu, L. Zhou, H. Yao, *Nanoscale* **2016**, *8*, 5254.

[136] Z. Yang, Z. Zhu, J. Ma, D. Xiao, X. Kui, Y. Yao, R. Yu, X. Wei, L. Gu, Y. S. Hu, H. Li, X. Zhang, *Adv. Energy Mater.* **2016**, *6*, 1600806.

[137] L. Luo, B. Liu, S. Song, W. Xu, J.-G. Zhang, C. Wang, *Nat. Nanotechnol.* **2017**, *12*, 535.

[138] L. Zou, Y. He, Z. Liu, H. Jia, J. Zhu, J. Zheng, G. Wang, X. Li, J. Xiao, J. Liu, J.-G. Zhang, G. Chen, C. Wang, *Nat. Commun.* **2020**, *11*, 3204.

[139] Z. Wang, D. Santhanagopalan, W. Zhang, F. Wang, H. L. Xin, K. He, J. Li, N. Dudney, Y. S. Meng, *Nano Lett.* **2016**, *16*, 3760.

[140] Y. Nomura, K. Yamamoto, T. Hirayama, M. Ohkawa, E. Igaki, N. Hojo, K. Saitoh, *Nano Lett.* **2018**, *18*, 5892.

[141] C. Zhu, R. Shao, S. Chen, R. Cai, Y. Wu, L. Yao, W. Xia, M. Nie, L. Sun, P. Gao, H. L. Xin, F. Xu, *Small Methods* **2019**, *3*, 1900061.

[142] X. Li, L. Zhao, P. Li, Q. Zhang, M. S. Wang, *Nano Energy* **2017**, *42*, 122.

[143] Z. Zeng, P. Barai, S. Y. Lee, J. Yang, X. Zhang, W. Zheng, Y. S. Liu, K. C. Bustillo, P. Ercius, J. Guo, Y. Cui, V. Srinivasan, H. Zheng, *Nano Energy* **2020**, *72*, 104721.

[144] H. Huang, J. Wang, X. Yang, R. Hu, J. Liu, L. Zhang, M. Zhu, *Angew. Chem.* **2020**, *132*, 14612.

[145] Y. A. Wu, Z. Yin, M. Farmand, Y. S. Yu, D. A. Shapiro, H. G. Liao, W. I. Liang, Y. H. Chu, H. Zheng, *Sci. Rep.* **2017**, *7*, 42527.

[146] S. Ahmed, M. Bianchini, A. Pokle, M. S. Munde, P. Hartmann, T. Brezesinski, A. Beyer, J. Janek, K. Volz, *Adv. Energy Mater.* **2020**, *10*, 2001026.

[147] A. K. Shukla, C. Ophus, C. Gammer, Q. Ramasse, *Microsc. Microanal.* **2016**, *22*, 494.

[148] L. Kovarik, A. Stevens, A. Liyu, N. D. Browning, *Appl. Phys. Lett.* **2016**, *109*, 164102.

[149] B. L. Mehdi, A. Stevens, L. Kovarik, N. Jiang, H. Mehta, A. Liyu, S. Reehl, B. Stanfill, L. Luzi, W. Hao, L. Bramer, N. D. Browning, *Appl. Phys. Lett.* **2019**, *115*, 063102.

[150] A. Stevens, L. Kovarik, P. Abellan, X. Yuan, L. Carin, N. D. Browning, *Adv. Struct. Chem. Imaging* **2015**, *1*, 10.

[151] Y. He, X. Ren, Y. Xu, M. H. Engelhard, X. Li, J. Xiao, J. Liu, J. G. Zhang, W. Xu, C. Wang, *Nat. Nanotechnol.* **2019**, *14*, 1042.

[152] L. Zhang, T. Yang, C. Du, Q. Liu, Y. Tang, J. Zhao, B. Wang, T. Chen, Y. Sun, P. Jia, H. Li, L. Geng, J. Chen, H. Ye, Z. Wang, Y. Li, H. Sun,

2300103 (19 of 20)

X. Li, Q. Dai, Y. Tang, Q. Peng, T. Shen, S. Zhang, T. Zhu, J. Huang, *Nat. Nanotechnol.* **2020**, *15*, 94.

[153] T. L. Burnett, P. J. Withers, *Nat. Mater.* **2019**, *18*, 1041.

[154] R. Moroni, M. Börner, L. Zielke, M. Schroeder, S. Nowak, M. Winter, I. Manke, R. Zengerle, S. Thiele, *Sci. Rep.* **2016**, *6*, 30109.

[155] M. T. M. Pham, J. J. Darst, D. P. Finegan, J. B. Robinson, T. M. M. Heenan, M. D. R. Kok, F. Iacoviello, R. Owen, W. Q. Walker, O. V. Magdysyuk, T. Connolley, E. Darcy, G. Hinds, D. J. L. Brett, P. R. Shearing, *J. Power Sources* **2020**, *470*, 228039.

[156] M. Lu, F. Yu, Y. Hu, K. Zaghib, S. B. Schougaard, Z. Wang, J. Zhou, J. Wang, J. Goodenough, T. K. Sham, *Chem. Commun.* **2020**, *56*, 984.

[157] A. Chambolle, T. Pock, *Acta Numer.* **2016**, *25*, 161.

[158] E. Y. Sidky, J. H. Jorgensen, X. Pan, *Phys. Med. Biol.* **2012**, *57*, 3065.

[159] M. Lustig, D. Donoho, J. M. Pauly, *Magn. Reson. Med.* **2007**, *58*, 1182.

[160] A. Stevens, L. Luzi, H. Yang, L. Kovarik, B. L. Mehdi, A. Liyu, M. E. Gehm, N. D. Browning, *Appl. Phys. Lett.* **2018**, *112*, 043104.

[161] K. Kunisch, T. Pock, *SIAM J. Imaging Sci.* **2013**, *6*, 938.

[162] F. Sherry, M. Benning, J. C. De Los Reyes, M. J. Graves, G. Maierhofer, G. Williams, C. B. Schönlieb, M. J. Ehrhardt, *IEEE Trans. Med. Imaging* **2020**, *39*, 4310.

[163] A. Stevens, H. Yang, L. Carin, I. Arslan, N. D. Browning, *Microscopy* **2014**, *63*, 41.

[164] B. Zhu, J. Z. Liu, S. F. Cauley, B. R. Rosen, M. S. Rosen, *Nature* **2018**, *555*, 487.

[165] J. Adler, O. Öktem, *IEEE Trans. Med. Imaging* **2018**, *37*, 1322.

[166] K. H. Jin, M. T. McCann, M. Unser, *IEEE Trans. Image Process.* **2017**, *26*, 4509.

[167] S. Arridge, P. Maass, O. Öktem, C. B. Schönlieb, *Acta Numer.* **2019**, *28*, 1.

[168] H. Li, J. Schwab, S. Antholzer, M. Haltmeier, *Inverse Probl.* **2020**, *36*, 065005.

[169] T. A. Bubba, G. Kutyniok, M. Lassas, M. März, W. Samek, S. Siltanen, V. Srinivasan, *Inverse Probl.* **2019**, *35*, 064002.

[170] S. Lunz, O. Öktem, C. B. Schönlieb, *Adv. Neural Inf. Process. Syst.* **2018**, *201-8-Decem*, 8507.

[171] P. Song, L. Weizman, J. F. C. Mota, Y. C. Eldar, M. R. D. Rodrigues, *IEEE Trans. Med. Imaging* **2020**, *39*, 621.

[172] M. J. Ehrhardt, M. M. Betcke, *SIAM J. Imaging Sci.* **2016**, *9*, 1084.

[173] M. J. Ehrhardt, in *Handbook of Mathematical Models and Algorithms in Computer Vision and Imaging: Mathematical Imaging and Vision* (Eds: K. Chen, C.-B. Schönlieb, X.-C. Tai, L. Younces), Springer International Publishing, Cham **2021**, p. 1.

[174] L. Bungert, M. J. Ehrhardt, *IEEE Access* **2020**, *8*, 222944.

[175] S. R. Arridge, M. J. Ehrhardt, K. Thielemans, *Philos. Trans. R. Soc., A* **2021**, *379*, 20200205.

[176] T. Schuster, B. Hahn, M. Burger, *Inverse Probl.* **2018**, *34*, 040301.

[177] B. Tremoulheac, N. Dikaios, D. Atkinson, S. R. Arridge, *IEEE Trans. Med. Imaging* **2014**, *33*, 1689.

[178] A. Hauptmann, O. Öktem, C. Schönlieb, in *Handb. Math. Model. Algorithms Comput. Vis. Imaging*, Springer International Publishing, Cham **2021**, pp. 1.

[179] Z. Jiang, J. Li, Y. Yang, L. Mu, C. Wei, X. Yu, P. Pianetta, K. Zhao, P. Cloetens, F. Lin, Y. Liu, *Nat. Commun.* **2020**, *11*, 2310.

[180] M. Smirnov, T. Garrett, R. Yasuda, *PLoS One* **2018**, *13*, e0199589.

[181] H. Xu, J. Zhu, D. P. Finegan, H. Zhao, X. Lu, W. Li, N. Hoffman, A. Bertei, P. Shearing, M. Z. Bazant, *Adv. Energy Mater.* **2021**, *11*, 2003908.

[182] I. M. Robertson, C. A. Schuh, J. S. Vetrano, N. D. Browning, D. P. Field, D. J. Jensen, M. K. Miller, I. Baker, D. C. Dunand, R. Dunin-Borkowski, B. Kabius, T. Kelly, S. Lozano-Perez, A. Misra, G. S. Rohrer, A. D. Rollett, M. L. Taheri, G. B. Thompson, M. Uchic, X. L. Wang, G. Was, *J. Mater. Res.* **2011**, *26*, 1341.

[183] Y. Guo, Y. Jiang, Q. Zhang, D. Wan, C. Huang, *J. Power Sources* **2021**, *506*, 230052.

[184] J. Billaud, F. Bouville, T. Magrini, C. Villevieille, A. R. Studart, *Nat. Energy* **2016**, *1*, 16097.

[185] J. S. Sander, R. M. Erb, L. Li, A. Gurijala, Y. M. Chiang, *Nat. Energy* **2016**, *1*, 16099.

[186] S. H. Lee, C. Huang, C. Johnston, P. S. Grant, *Electrochim. Acta* **2018**, *292*, 546.

[187] J. M. Warnett, V. Titarenko, E. Kiraci, A. Attridge, W. R. B. Lionheart, P. J. Withers, M. A. Williams, *Meas. Sci. Technol.* **2016**, *27*, 035401.